UNIVERSITY OF TARTU
Faculty of Science and Technology
Institute of Chemistry

Huy Qui Vinh Nguyen

OXYGEN REDUCTION ON PLATINUM NANOPARTICLES DEPOSITED ONTO CHROMIUM CARBIDE DERIVED CARBON SUPPORT

Master's Thesis (30 ECTS)
Curriculum: Applied Measurement Science

Supervisors: Ph.D. Jaak Nerut
Ph.D. Heili Kasuk

Tartu 2019

Hapniku redutseerimine kroomkarbiidist sünteesitud süsinikule sadestatud plaatina nanoosakestel

Polümeer-elektrolüüt-membraan kütuseelemendid on efektiivsed energia muundamise seadmed, mida kasutatakse juba ühistranspordis. Laialdasemat kasutusele võttu piirab aeglane hapniku redutseerumise reaktsioon (ORR) katoodil ning seetõttu tuleb selles katalüsaatorite vallas arendustegevust jätkata. Töö eesmärgiks oli sünteesida uus alusmaterjal plaatina katalüsaatorile ning uurida ORR-i uuel katalüsaatormaterjalil. Süsinikkandjad sünteesiti kroomkarbiidist kasutades kloreerimist erinevatel temperatuuridel (800-900°C). Plaatina sadestamiseks süsinikkandjale kasutati kahte meetodit. Alusmaterjali ja katalüsaatori struktuuri kindlaks tegemiseks kasutati termogravimeetria, röntgendifraktsioonanalüüsi ja lämmastiku madalatemperatuurse adsorptsiooni/desorptsiooni meetodeid. ORR uurimiseks rakendati tsüklilise voltammeetria ja pöörleva ketaselektroodi meetodeid. Katalüsaatorite ORR aktiivsus 0.1 M $HClO_4$ lahuses oli hea.

***Märksõnad*:** karbiidset päritolu süsinik, hapniku redutseerimine, plaatina katalüsaator, kroomkarbiid, süsinikkandja.

***CERCS kood*:** P401 Elektrokeemia

Oxygen reduction on platinum nanoparticles deposited onto chromium carbide-derived carbon support

Polymer electrolyte membrane fuel cells are very promising energy conversion devices, which have already found application in public transportation. However, one of the obstacles in the even wider application is the sluggishness of oxygen reduction reaction (ORR) at the cathode. Therefore, there is room for development in the field of catalysis synthesis. This study aimed to develop novel carbon support material for the platinum catalyst and to study ORR on the new catalyst. The carbon supports were synthesized from chromium carbide using chlorination at various temperatures (800-900°C). The platinum nanoparticles were deposited onto the chromium carbide-derived carbon supports by two different methods. Thermogravimetric analysis, X-ray diffraction and low-temperature nitrogen adsorption/desorption methods were used to characterize the structure of catalyst and catalyst support. ORR was studied with cyclic voltammetry and rotating disk electrode methods. The catalysts showed high activity towards ORR in 0.1 M $HClO_4$ solution.

***Keywords*:** carbide-derived carbon, oxygen reduction reaction, platinum catalysts, chromium carbide, carbon support

***CERCS code*:** P401 Electrochemistry

TABLE OF CONTENTS

1. INTRODUCTION

Green energy gains huge attention recently as the demand for finding sustainable and alternative energy for fossil fuels is becoming more and more essential. The promising technology for alternative-green energy is a polymer electrolyte membrane fuel cell (PEMFC), which converts chemical energy stored in hydrogen (and oxygen) molecules directly into electrical energy and produces only water as a byproduct. PEMFC applications are widely found in vehicle engines, energy station, and power banks for mobile devices. For example, in rural regions where the electric grids are unreachable, the solar system combined with PEMFC energy storage is the right solution.

Benefits of PEMFCs on the environment are apparent. However, many barriers are preventing the commercialisation and spread usage of PEMFCs. For instance, the cost for generating power energy of 1 kW and lifetime of PEMFCs should be competitive with internal combustion engines. It is not merely for solving the problem because there are various interrelated and complex phenomena such as mass/heat transfer, electrochemical reactions, ionic/electronic transport when the fuel cell is operating. The oxygen reduction reaction (ORR) at the cathode of PEMFC is somewhat sluggish and slow. Besides, the breakthroughs of the cost and durability are crucial factors. Therefore, considerable research is taking place in the field of PEMFC catalysts and construction.

The stability and catalytic activity of the ORR catalyst are critical. The catalyst supports play a very often crucial role. Catalyst support, which is stable in a wide potential region and has a high surface area, could improve the ORR kinetics. Therefore, extensive research is done in the field of catalyst supports.

The aims of this work were:

- Synthesise carbon supports from chromium carbide (Cr_3C_2) under specific syntheses temperatures (800-1100 °C) and deposit platinum nanoparticles onto these carbon supports.
- Perform physical characterisations of carbon supports C(Cr_3C_2) and platinum catalysts Pt-C(Cr_3C_2).
- Investigate the ORR on C(Cr_3C_2) and Pt-C(Cr_3C_2) in 0.1M $HClO_4$ solution.

2. LITERATURE OVERVIEW

2.1. Classification of fuel cells

Fuel cells convert chemical energy into electricity. Depending on the type of fuel or electrolyte used in the fuel cell, the fuel cells may be classified as follows: [1]

- PEMFC is the assembly of a water-based acidic polymer membrane and platinum-based electrodes. This fuel cell consumes pure hydrogen gas and releases only water as a byproduct. The working temperature is 40-100 °C.
- High-temperature PEMFC (HT−PEMFC) is a PEMFC with a mineral acid-based electrolyte instead of a water-based electrolyte. HT-PEMFC operating temperature is up to 200 °C.
- Direct methanol fuel cell (DMFC) is in a subcategory of PEMFCs, which uses methanol as fuel. Electrodes are platinum-ruthenium catalysts supported onto carbon. A polymer membrane is an electrolyte. The operating temperature is from 40 to 100 °C.
- Molten carbonate fuel cell (MCFC) consists of liquid molten carbonate salts as an electrolyte and of an electrode matrix, which is made from nickel and nickel oxide. MCFC consumes methane and natural gas. The operating temperature is around 650 °C.
- Phosphoric acid fuel cell (PAFC) consists of carbon electrodes with finely dispersed platinum as a catalyst. Phosphoric acid is used as an electrolyte in PAFC. Operating temperature is in the range of 150-220 °C.
- Solid oxide fuel cell (SOFC) is operating at very high temperatures at around 1000 °C. SOFC electrodes are based on perovskite and perovskite/metal cermet and electrolyte is based on metallic oxide solid ceramic. The mixture H_2/CO is used as fuel.
- Electrodes of the alkaline fuel cell (AFC) consist of transition metals and from platinum as a catalyst. Potassium hydroxide is used as the electrolyte. Pure hydrogen and oxygen are used as a fuel for AFC. The working temperature is 65-220 °C.

2.2. PEMFC

The membrane electrode assembly (MEA) consists of a polymer electrolyte membrane in contact with anode and cathode (**Fig.** 1). The electrodes are composed of a gas diffusion layer and catalyst layer, which commonly is carbon support with a platinum catalyst.

The PEMFC efficiency depends highly from the Pt catalyst. Although the ORR at cathode catalyst layer (CL) and hydrogen oxidation reaction (HOR) at anode CL of fuel cell have distinguishable electrochemical activities, Pt catalysts are still the best candidates for both cathodic and anodic catalysts [2]. Anodic catalyst is expected to possess an excellent ability to tolerate CO. CO poisoning effect blocks the active site on the Pt surface and reduces the reactivity. Cathodic catalysts have more requirements due to the sluggishness of ORR, which is discussed more detailed in the catalyst and ORR sections.

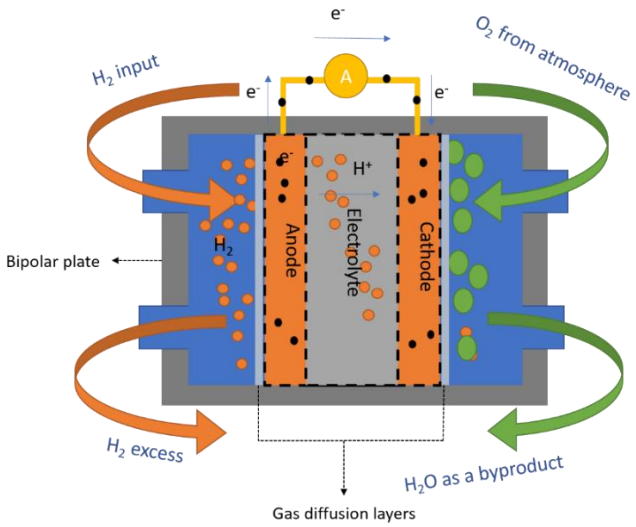

Figure 1. A PEMFC scheme for a single cell.

The polymer electrolyte membrane is located in the middle part between the anode and cathode electrodes to insulate electricity and prevent oxygen reactants from travelling across the membrane layer to the anode side. The thin membrane plays the role of proton/ion transport layer, which transfers hydrogen ions from anode to cathode side. Depending on the used material for fabrication, the thickness of membranes varies from 10–100 μm [3]. The membranes should tolerate the operating temperature, mechanical tension, and a chemical environment, e.g. the formation of OH− and HOO radicals. Perfluorosulfonic acid is the most popular substance for membranes, also known as Nafion®. Polytetrafluoroethylene (PTFE) contributes to the physical strength of the Nafion® membrane, and sulfonic acid groups work as proton transport sites. Other perfluorinated-based materials suit the purpose of fuel cell applications such as Gore-Select™, Flemion™, Asiplex™ [3,4].

Gas diffusion layers (GDL) are located between the bipolar plate (BP) and the catalyst layer. GDL is usually porous carbon paper with the thickness 100-300 μm. GDL distributes the gases to the catalyst layers, and GDL is electrical contact between electrodes and facilitates water transportation in the system. GDL improves the efficiency of gas diffusion and reduces mass transport overpotential [2,3].

PEMFC working principle is based on HOR and ORR processes. In HOR, the hydrogen gas is split into hydrogen ions and electrons at the anode CL (**Eq.** 1). After that, hydrogen ions travel through the membrane to the cathode CL. The electrons produced at HOR move through an external circuit and travel to the cathode CL. Simultaneously, oxygen shifts through the GDL and reaches the cathode CL. At cathode CL, the ORR occurs and produces water and heat.

Water can travel back to the cathode side and through the membrane to the anode side due to the differences in water concentration and pressure between anode and cathode site [5].

$$H_2 \longrightarrow 2H^+ + 2e^- \quad \textbf{(Eq. 1)}$$

2.3. PEMFC catalysts (general overview)

The critical function of the catalyst is to increase the ORR rate in the cathode CL. Since Pt is a preferred metal used in both anode and cathode, it contributes significantly to the cost of the CL and fuel cell [3]. Therefore, one of the goals for researches is to minimise the amount of Pt used. Firstly, various Pt-metal alloys were investigated, and high electrochemical activities were achieved. Other less expensive precious metals, e.g. ruthenium and palladium [6,7] were studied. Finally, a new class of heteroatomic polymer nanocomposite catalyst with non-precious metals was demonstrated its suitability for PEMFC cathode [8].

To diminish the cost of catalyst, an abundance of support materials is tested. In order to obtain a high catalytic material, the general requirements for support materials are [9].

- The maximum dispersion enhances electron transfer and diffusion of species. Therefore, support materials with a specific area larger than 100 $m^2\ g^{-1}$ allow better dispersions of Pt nanoparticles [10].
- For safety reason, support materials should have low flammability under PEMFC working conditions.
- Chemical and electrochemical properties of the catalyst layer should be stable during the operating time.
- Catalyst layer should have a high proton and electric conductivity.
- Other considerations. Materials with suitable porosity, high crystallinity and large surface area facilitate the best dispersion of Pt nanoparticles.

The dispersion of Pt nanoparticles is affected dramatically by deposition techniques and properties of catalyst supports. Techniques for deposition of catalyst nanoparticles onto the catalyst supports are investigated many authors [11,12]. In general, there are several techniques such as impregnations, ultrasound, polyol and microwave-assisted polyol, electrochemical depositions, colloidal-based techniques, sputter depositions, precipitations and ion-exchange [13]. The study by Sebastián et al. demonstrated that the Pt nanoparticles dispersed on their support material using colloidal synthesised route had a smaller size (2.5 nm) than 8.1 nm for impregnation method [14]. According to the study of Li et al. [15], colloidal-based techniques are more controllable for suitable Pt nanoparticle size than impregnations and precipitation

techniques. The structure of the support materials may control the dispersion of Pt in the impregnations, and precipitation techniques since the Pt nanoparticle size in colloidal-based techniques is influenced mostly by protecting agents [16–18].

2.4. PEMFC Pt-catalysts

Pt-based catalysts are used widely in PEMFC applications. The morphological study of Pt nanoparticles is usually performed by either scanning electron microscopy (SEM) or transmission electron microscopy (TEM). The particle size of Pt affects the performance and durability of fuel cells [19]. A smaller Pt particle size exhibited lower durability, which was investigated by using load cycles method. The increment in Pt particle size could provide higher Pt surface area for the adsorption of oxygen and improve the durability of the PEMFC. However, there are studies which prove that Pt nanoparticles with a size of approximately 2 nm exhibit higher mass activity and durability [20,21]. According to Li et al. [19], a suitable catalyst should have a narrow nanoparticle size distribution, a high surface area and excellent dispersion of platinum on the support material.

Mayrhofer et al. described the effect of Pt particle size on the ORR performance [22,23]. The study indicated that decreasing the particle size increases the surface covering with oxygen groups and causes the increase of the zero charge potential. Electroactive species with high oxophilicity can block the active site and inhibit oxygen adsorption. However, there are many studies, which agree that the Pt particles with size 2-4 nm are the most active towards ORR [20,24–27].

Since the size of the Pt particle influences the fuel-cell performance strongly, it is crucial to optimise the Pt particle size during the synthesis [13]. In the Pt synthesis, there are a few popular precursors, e.g. hexachloroplatinic acid, tetraammineplatinum (II) chloride, and ammonium hexachloroplatinate. Precursors are hydrophilic compounds and decompose at a temperature of 320-375 °C [28,29]. Synthesised techniques, which mentioned above in the PEMFC catalysts section, are possible to apply to get a desirable Pt particle size. In the polyol technique, ethylene glycol is a well−known reducing agent, which demonstrated to get a smaller particle size and a better dispersion on the support material [30–33]. Heat treatment tends to increase the Pt particle size, and it gives an abnormal dispersion [34].

2.5. Oxygen reduction reaction

One of the most critical points in the studies of PEMFC and the commercialisation of PEMFC is the ORR at the cathode. The ORR mechanism is determined by the electrode material composition and by the environment.

Commonly, carbon-supported platinum was a successful candidate for ORR studies because of the structural sensitivity of oxygen adsorption [35] and oxygen reduction on Pt [36]. The ORR can proceed on Pt catalyst material in either alkaline or acidic environments, depending on the purposes of the application. The reaction pathways can be either through 2-electrons or 4-electron transfer. The 2-electron pathway creates intermediates like hydrogen peroxide that decrease the catalytic activity of cathode. The 2-electron process is proceeded by the reduction to water or decomposition of peroxide [37].

ORR in the alkaline environment can be described with the following overall chemical reaction and standard electrode potential values E^0 at 25°C [37]:

$$O_2 + H_2O + 4e^- \rightarrow 4OH^- \qquad E^0 = 0.401\ \text{V}\ (\textbf{Eq}.\ 2)$$

Simultaneously the second pathway is possible:

$$O_2 + H_2O + 2e^- \rightarrow HO_2{}^- + OH^- \qquad E^0 = -0.065\ \text{V}\ (\textbf{Eq}.\ 3)$$

$$HO_2{}^- + H_2O + 2e^- \rightarrow 3OH^- \text{ or} \qquad E^0 = 0.867\ \text{V}\ (\textbf{Eq}.\ 4)$$

$$2HO_2{}^- \rightarrow 2OH^- + O_2 \qquad (\textbf{Eq}.\ 5)$$

ORR in the acidic solution can be described with the following overall chemical reaction [37]:

$$O_2 + 4H^+ + 4e^- \rightarrow H_2O \qquad E^0 = 1.229\ \text{V}\ (\textbf{Eq}.\ 6)$$

Alternatively, through hydrogen peroxide intermediate:

$$O_2 + 2H^+ + 2e^- \rightarrow H_2O_2 \qquad E^0 = 0.67\ \text{V}\ (\textbf{Eq}.\ 7)$$

Hydrogen peroxide is reduced or decomposed to water [37]:

$$H_2O_2 + 2H^+ + 2e^- \rightarrow 2H_2O \qquad E^0 = 1.77\ \text{V}\ (\textbf{Eq}.\ 8)$$

$$2H_2O_2 \rightarrow 2H_2O + O_2 \qquad (\textbf{Eq}.\ 9)$$

Researchers proposed many models for ORR due to the lacking knowledge of intermediate species and competing pathways. However, a widely accepted ORR model in the acidic aqueous solution is showed in the figure (**Fig.** 2) [38].

In **Fig.** 2, oxygen can be reduced either directly to the water with a 4-electron process, and with the rate constant k_1, or through the formation of hydrogen peroxide ($H_2O_{2\ ads}$) as a with a 2-electron

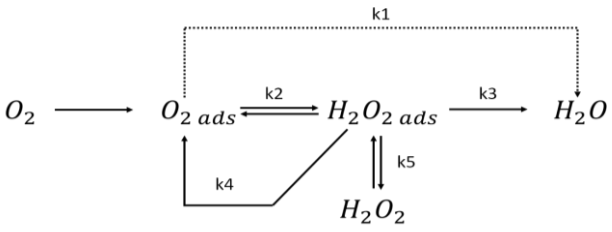

Figure 2. ORR in the acidic environment [37].

process, with the rate constant k_2. $H_2O_{2\ ads}$ can be reduced further to water (with rate constant k_3) or decomposed at electrode surface to oxygen (with rate constant k_4). Additionally, $H_2O_{2\ ads}$ can also diffuse into the electrolyte with the rate constant k_5 [38].

ORR mechanisms on specific materials are different and depend on the catalyst's support material structure and from the catalytic activity of the material but also from the pH of the electrolyte [37]. The detailed mechanism of ORR on graphite electrode is proposed by Taylor and Humffray [39] (**Eq**. 10-12). The first electron transfer was assumed as the rate-determining step (RDS) [40]. Taylor and Humffray also demonstrated that the RDS depends on the electrolyte pH value [39,41].

$$O_2 \rightarrow O_{2\ ads} \qquad \textbf{(Eq. 10)}$$

The "*ads*" subscript is denoted for corresponding absorbed species on the electrode surface.

$$O_{2\ ads} + e^- \rightarrow O_{2\ ads}^- \qquad \textbf{(Eq. 11)}$$

After receiving an electron, $O_{2\ ads}^-$ is protonated in the solution (pH < pK_a(HO_2) ~ 4.8).

$$O_{2\ ads}^- + H_2O \rightarrow O_2 + HO_2^- + OH^- \qquad \textbf{(Eq. 12)}$$

Mechanism of ORR on glassy carbon (GC) was proposed by Yeager [42] (**Eq**. 13-18). At pH < 10, the reaction (**Eq**. 14) is the RDS [39], and the reaction (**Eq**. 15) is the RDS at pH >10 [41]:

$$O_2 \rightarrow O_{2\ ads} \qquad \textbf{(Eq. 13)}$$

$$O_{2\ ads} + e^- \rightarrow [O_{2\ ads}^-] \qquad \textbf{(Eq. 14)}$$

$$[O_{2\ ads}^-] \rightarrow \{O_{2\ ads}^-\} \qquad \textbf{(Eq. 15)}$$

$$\{O_{2\ ads}^-\} + HOH \rightarrow HO_{2\ ads} + OH^- \qquad \textbf{(Eq. 16)}$$

$$HO_{2\ ads} + e^- \rightarrow HO_{2\ ads}^- \qquad \textbf{(Eq. 17)}$$

$$HO_{2\ ads}^- \rightarrow HO_2^- \qquad \textbf{(Eq. 18)}$$

In the reaction (**Eq**. 15), the reactant and product are two different superoxide ions on the carbon surface. The reactant, in this case, is the inert absorbed form at the inert carbon site, but the product indicates the migration of the same species to the active site.

In Pt catalysts, the dissociative and associative routes were proposed for different current ranges [43,44]. The RDS are reactions (**Eq**. 20 and **Eq**. 23).

In dissociative route (from **Eq**. 19-21) the O_2 is broken up before the RDS [44]:

$$O_2 + 2Pt \rightleftharpoons 2PtO \qquad \textbf{(Eq. 19)}$$

$$PtO + H^+ + e^- \rightleftharpoons PtOH \qquad \textbf{(Eq. 20)}$$

$$PtOH + H^+ + e^- \rightleftharpoons Pt + H_2O \qquad \textbf{(Eq. 21)}$$

In this pathway, the adsorption of oxygen to the Pt clusters breaks the superoxo state of oxygen (O-O bond) to form adsorbed atomic O [35], which is gains two electrons to produce water. Peroxide cannot be formed with this route because of no adsorbed O_2 on Pt site. This pathway can be considered as the direct route for the 4-electron pathway.

In the associative route of ORR, the O_2 is broken up after the RDS (**Eq**. 22-26) [44]:

$$O_2 + Pt \rightleftharpoons PtO_2 \quad \text{(Eq. 22)}$$

$$PtO_2 + H^+ + e^- \rightleftharpoons PtOOH \quad \text{(Eq. 23)}$$

$$PtOOH + H^+ + e^- \rightleftharpoons PtOH + OH \quad \text{(Eq. 24)}$$

$$PtOH + OH + H^+ + e^- \rightleftharpoons PtOH + H_2O \quad \text{(Eq. 25)}$$

$$PtOH + H^+ + e^- \rightleftharpoons Pt + H_2O \quad \text{(Eq. 26)}$$

The associative route does not include the formation of peroxide and follows the *peroxo mechanism*, described with equations **Eq**. 24-26 [44]. In detail, when the adsorbed O_2 is presented on Pt site, O-O bond may be not broken. As a result, H_2O_2 is formed. The H_2O_2 can be a final product or be reduced to form H_2O. In that case, the mechanism can be expressed as in **Fig.** 2 [36].

Kinetics of the reaction (**Eq**. 27), which forms or reduces OH from/to water, is so fast and becomes equilibrium during ORR. OH was considered as the leading cause of blocking intermediates at sites, and this effect was used to explain large overpotentials observed on even the best catalysts [45,46]. The site-blocking hypothesis was concerned by many researchers to improve the site accessibility of new catalysts [47–49]:

$$H_2O + * \leftrightarrows OH* + H^+ + e^- \quad \text{(Eq. 27)}$$

2.6. Catalyst supports

In the PEMFC application, two categories of catalyst supports are used: carbon and non-carbon-based support material. In this study, the carbon-based catalyst support was used. Carbon support is widely used because of its very high surface area to obtain high metal dispersion, optimal porosity for quick mass transport, high electric conductivity, and stability under the working environment of PEMFCs. Many interesting nanostructures of carbon such as mesoporous carbons, carbon nanotubes, carbon nanofiber, nanodiamonds, graphite, graphene, and hetero-doped atoms in carbon-based support have been tested in several works and are suitable for PEMFC application [9,50].

Carbon black is one of the most popular catalysts supports for PEMFCs, especially for Pt and Pt-based catalysts. The carbon black particles have a spherical shape with a diameter of

less than 50 nm [51]. However, the structure of carbon black is thermo-chemically unstable in PEMFC working condition. The impurities in carbon black [51] may affect negatively to ORR on Pt catalyst because of the sensitivity of platinum to the impurities in ORR [36].

Carbon nanotubes (CNTs) structure [9], and the morphology can be controlled well in chemical vapour deposition [52]. In comparison with carbon black, CNTs exhibit higher surface area, better electric conductivity, higher stability under operation condition and a lower amount of impurities than in carbon black [9]. Multiple-walled CNTs exhibited better ORR activity and fuel cell performance than the commercial Pt-C materials due to better mass transport and electron transfer [53–55].

The surficial morphology of carbon and catalyst dispersion may affect catalyst activity directly. For example, catalyst nanoparticles could dive into micropores of carbon black, which prevent the catalyst contact with reactants and therefore, reduce the ORR activity [51]. It is also considered that the increment of oxygen groups on the surface of carbon material improves the dispersion of the catalyst and catalyst activity [50]. The insufficient number of active sites for binding causes abnormal dispersion and agglomeration of catalyst. Many mesoporous carbons with a high number of oxygen groups on the surface increase the dispersion of catalyst due to a better binding of carbon surface and metal catalysts [56]. The large microporous surface provided an excellent ORR performance due to the increment of active site density [57].

Pretreatments of carbon before catalyst deposition for obtaining more binding sites are necessary and widely implemented [11,56,58]. Smaller Pt nanoparticles were formed on the surface of the carbon after acid treatment in comparison with the same untreated carbon [59].

2.6.1. Carbide-derived carbons

Excellent carbon support material with controlled bimodal pore size and high specific surface area can be synthesised from metal carbides. Carbide-derived carbons (CDC) can be synthesised from carbide precursors, mainly from the binary or ternary carbides, using the high-temperature etching method in halogen gas environment or hydrothermal method [60].

The formation of micro- and mesoporous structure is caused mainly by the chemical properties and the structure of precursor [61]. In the synthesis of CDCs by using chlorination, it is possible to control the porosity in atomic level by optimizing parameters of chlorination such as chlorination temperature [62–65], chlorine concentration [66], etching reagent [67,68], annealing [69], catalyst [70,71], and post-synthesized treatment [72].

A general reaction to synthesise CDCs [73]:

$$M_xC_y + \frac{xz}{2}Cl_2 \rightarrow xMCl_z + yC \quad \textbf{(Eq. 28)}$$

where M stands for different elements from the carbide. T. Thomberg et al. [73], synthesised CDC from different types of chromium carbide powders by chlorination at specific temperatures from 800 °C to 1100 °C. In the final step, residues of the halogenated and oxygenated groups from the CDC surface were removed by treatment with H_2 / Ar at 800 °C for 1.5 hours. The C(Cr_3C_2) and C(Cr_7C_3) carbon materials have micro/mesoporous structures; however, the amount of micropores is small due to the long-lasting byproducts removing step. The bimodal pore size distributions are exhibited with the pore size distribution around 2.5-3.5 nm and from 6-8 nm. Compared to other materials synthesized and studied by T. Thomberg et al., C(Cr_3C_2, 800 °C) has high specific surface area (270 $m^2\ g^{-1}$) and the highest microporous area (S_{micro}=102 $m^2\ g^{-1}$) and volume (V_{micro}=0.057 $cm^3\ g^{-1}$), the average pore size was 4.7 nm. Therefore, this material is a good candidate for PEMFC studies [12].

2.7. Deposition of catalyst layer on glassy carbon disk electrodes

In order to measure the electrochemical activity of the material, catalyst ink suspension has to be prepared and deposited onto the electrode. Many factors are affecting the ORR kinetics such as impurities, measuring protocols, and measurement correction. However, the influences of catalyst ink and catalyst layer on the glassy carbon disk electrode have an essential role in improving the measured ORR activity.

Ikuma Takahashi et al. [74] sonicated a few times the proportion of water and isopropanol (isopropyl alc., IPA) to optimise IPA content. The catalyst inks, prepared with the optimal IPA, presented approximately 20% higher electrochemical activities (ECAs) than IPA-free inks [74].

The material dispersion quality onto the electrode surface affects enormously the parameters measured using electrochemical methods. The catalyst suspension can be deposited onto the electrode using different methods like stationary (S) or rotational drying technique (RD) [75]. Using the rotational drying technique, the suspension is deposited onto the glassy carbon electrode at a very slow rotation rate before drying at the desired rotational rate. A typical structure, which is usually formed when depositing the catalyst suspension onto the electrode using the stationary techniques (S) is the “coffee ring” structure [76]. The “coffee ring” effect is suppressed significantly by using RD techniques. After depositing the catalyst suspension using RD technique, the specific activities (SA) at 0.9 V increase by a factor of 1.9 (without iR compensation) [76].

Watanabe et al. [77] illustrated that the <0.2 μm film thickness did not influence the limiting currents of H_2 and O_2 diffusion. A depositing/drying techniques were developed by Schmidt et al. [78], called TF-RDE, which includes of the serial of processes, depositing a drop of catalyst ink on the electrode surface, drying, and lastly creating a capped structure by putting a drop of Nafion® on the electrode. In their study, H_2 diffusion resistance is negligible when the Nafion® capped thickness is less than 0.5 μm. Paulus et al. [79] presented that O_2 diffusion resistance could be not of concern when the Nafion® capped thickness is below 0.2 μm. In conclusion, the calculated Nafion® cap thickness has no measurable effects on O_2 limiting currents if it is less than or in range of 0.1−0.2 μm, but the effects of the ionomers on ORR kinetics should be of concern [79,80].

The influence of ink composition on the coverage of the electrode surface and electrode activity is well-known [80,81]. A high ratio of ionomer to carbon (*I/C*) can cause the flooding issue on the electrode surface, but a too low *I/C* ratio also results in incompletely coverage of the electrode surface.

In the study of Shinozaki et al. [75], they used Pt/V for studying the influences of catalyst inks, and depositing/drying techniques on ORR kinetics. The loadings of Pt nanoparticles in both Nafion®-based and Nafion-free ink composition were 18 $\mu g_{Pt}\ cm^{-2}$. The Nafion®-free ink composition exhibited three times higher mass activity (MA) and specific activity (SA). In case of Nafion®-based inks, RDE drying in the air (N-RAD) was more reproducible than the stationary drying in isopropanol vapour technique (N-SIPAD), which is more sensitive and depending on the specialist skills. From the conventional stationary air drying techniques, it is impossible to forecast the ORR trends accurately.

2.8. Rotating disc electrode method

The most common method to study the ORR mechanism and kinetics is the rotating disc electrode method (RDE) [11,12,82], where the working electrode is mounted to a rotator for the hydrodynamic voltammetry. The mass transfer of reactants takes place through three mechanisms: migration caused by the electric field gradient, convection due to the rotating of the electrode, and diffusion caused by the concentration differences at the surface of the working electrode and bulk solution [83]. The influence of migration on reacting species is usually suppressed by the usage of indifferent electrolyte in high excess. The solution near the electrode can be divided into the convection region and stagnant Nernst diffusion layer. The diffusion layer thickness, δ, is proportional to the rotation speed of the electrode [84]:

$$\delta = 1.61 D_{O_2}^{1/3} \nu^{1/6} \omega^{-1/2} \quad \textbf{(Eq. 29)}$$

where D_{O_2} is the diffusion coefficient of oxygen in the bulk solution, ν is kinematic viscosity of the bulk solution, and ω is the angular velocity of the rotating electrode. If the process is a mass-trasfer limited, the diffusion step limited charge transfer current density can be calculated with the Levich equation [84]:

$$i_d = -0.62 n \mathrm{F} D_{O_2}^{2/3} \nu^{-1/6} c_{O_2} \omega^{1/2} \quad \textbf{(Eq. 30)}$$

where F is Faraday constant, c_{O_2} the concentration of oxygen in the bulk solution, n is the number of electron transfer per one O_2 molecule. According to the Levich equation, the limiting current depends linearly from the bulk solution concentration. The oxygen diffusion coefficient value and the electron number may be calculated using **Eq**. 30.

If charge transfer and mass transfer steps limit the ORR process, the classical Koutechký-Levich (K-L) equation [85] can be applied.

$$\frac{1}{j} = \frac{1}{j_\mathrm{k}} + \frac{1}{j_\mathrm{d}} \quad \textbf{(Eq. 31)}$$

where j is the current density, $j_\mathrm{k} = -n\mathrm{F}k_\mathrm{het}c_{O_2}$ is kinetic current density, and k_het the electrochemical rate constant for ORR.

Nevertheless, it has been shown that for a thick Nafion film, mass-transport resistance on poly-Pt RDE disk covered with an ionomer film contributes an additional term $\frac{1}{j_\mathrm{f}}$ to the K-L equation.

$$\frac{1}{j_\mathrm{f}} = \frac{1}{-n\mathrm{F}D_\mathrm{f}C_\mathrm{f}/\delta_\mathrm{f}} \quad \textbf{(Eq. 32)}$$

where δ_f is the Nafion film thickness, D_f and C_f are the diffusivities and the solubility of oxygen in the film, respectively. K-L equation with the film resistance is written out in detail below [12,85]:

$$\frac{1}{j_\mathrm{c}} = \frac{1}{-n\mathrm{F}k_\mathrm{het}c_{O_2}} + \frac{1}{-0.62n\mathrm{F}D_{O_2}{}^{2/3}\nu^{-1/6}c_{O_2}\omega^{1/2}} + \frac{1}{-n\mathrm{F}D_\mathrm{f}C_\mathrm{f}/\delta_\mathrm{f}} \quad \textbf{(Eq. 33)}$$

In this study, c_{O_2} = 1.26 mol m^3 in 0.1 M $HClO_4$ solution at 25 °C [86], D_{O_2} = 1.90×10^{-5} cm^2 s^{-1} in 0.1 M $HClO_4$ solution at 25 °C [86], and ν (of 0.1 M $HClO_4$ solution) = 0.0089 cm^2 s^{-1} at 25 °C [87].

Using the above equations, it is possible to calculate the kinetic current density and the number of electrons transferred in the electrochemical reaction. The kinetic current density versus electrode potential plots are so-called Tafel plots. It is possible to get information about the ORR mechanism from the Tafel plot slopes.

3. EXPERIMENTAL

3.1. Synthesis and preparation of experiments

3.1.1. Synthesis of catalyst supports

Carbide-derived carbons from Cr_3C_2 (99.5% purity, −325 mesh powder, the product of Sigma-Aldrich) were synthesised by high-temperature chlorination process. Chromium carbide powder was reacted with a flow of chlorine gas (AGA, 99.99%) in a quartz stationary bed reactor at the desired temperature from 800 to 1100 °C. The flow rate of chlorine was controlled at 50 $cm^3\ min^{-1}$. The byproduct, $CrCl_3$, was eliminated by flowing chlorine, then excessive chlorine and byproduct gases were removed by flushing slowly with an Ar stream. Halogenated and oxygenated groups on the surface of carbon were removed using the mixture H_2/Ar (1:4) at 800 °C (H_2 >99.9999%, Model NMH_2 500, Linde Gas; Ar 99.999%, Linde Gas AGA).

3.1.2. Synthesis of platinum catalysts

The desired amount of platinum in the catalyst was 20 wt%. The platinum was deposited on carbon supports using two methods.

Firstly, Pt-nanoparticles were synthesised on C(Cr_3C_2, 800 °C) by ultrasound assisted incipient wetness impregnation (UIGR) [13] of $H_2PtCl_6{\times}6H_2O$ solution in ethanol and gas phase reduction under H_2/Ar atmosphere. In detail, a mixture of $H_2PtCl_6{\times}6H_2O$ (99.9%, Alfa Aesar) and C(Cr_3C_2, 800 °C) was mixed with 1 cm^3 of 99.5% ethanol (200 proof, anhydrous, Sigma-Aldrich). Impregnation was performed in an ultrasonic bath (Elmasonic P 30 H, Elma) at 100% power for 1 hour before the mixture was placed in the vacuum oven at 90 °C and 50 mbar to dry overnight. The powder was placed in a large quartz vessel for the gas reduction process. The mixture of H_2/Ar in volume ratio 3:7 flowed over the powder, so the flow rates were 15 $cm^3\ min^{-1}$ and 35 $cm^3\ min^{-1}$, respectively. Temperature program was controlled to rise 1 K min^{-1} from 25-135 °C. The temperature of the tube furnace was increased up to 135 °C, and the reaction mixture was kept at this temperature for three hours. Afterwards, the gas was switched to pure argon, and it waited until the furnace cooled down.

The second method for deposition Pt nanoparticles onto C(Cr_3C_2, 800 °C), C(Cr_3C_2, 900 °C), C(Cr_3C_2, 1000 °C) was ultrasound-microwave assisted ethylene glycol reduction (MWEG) [11,13] with $H_2PtCl_6{\times}6H_2O$ precursor (99.9%, Alfa Aesar). $H_2PtCl_6{\times}6H_2O$ and CDC were mixed with desired amount NaOH solution (99.99%, semiconductor grade, Sigma-Aldrich) and 100 cm^3 ethylene glycol solution (puriss. p.a., Reag. Ph. Eur., ≥99.5%, Honeywell). The amount of NaOH should be enough to adjust pH to 12 (tested by the indicator

paper). The 250 cm^3 beaker containing the mixture was covered by a piece of parafilm, and the mixture was sonicated in the ultrasonic bath for 30 min. Then, the beaker was covered with a Petri dish before microwaving at low-medium power to nearly boiling state (commercial 750W microwave). C(Cr_3C_2, 800 °C) and C(Cr_3C_2, 900 °C), were microwaved twice. The mixture was cooled down to room temperature before the second microwaving step started. C(Cr_3C_2, 1000 °C) was microwaved one time. After that, the mixture was cooled down to room temperature. At this stage, the pH was around 7-8 before topping up with 100 cm^3 of Milli-Q water. The mixture was stirred for 30 min before adjusting to pH 0 by concentrated nitric acid (65% G.R., the product of Lach-ner). It was stirred for 30 min before standing overnight for the sedimentation. Next morning, the mixture was filtrated with the Durapore® membrane filter (0.45 μm HV, Merck Millipore Ltd.) and a vacuum filtration system. After that, the filter and the sample were dried at 50 °C and 50 mbar before collecting the final material synthesised.

3.1.3. Preparation of catalyst suspension and electrodes

Specific suspension recipes and drying techniques were used for different types of materials.

In the case of the CDC electrodes, the carbon loading was 1 mg cm^{-2}, ionomer to carbon I/C (wt / wt) ratio was 0.07. Nafion®117 (~5% solution, Sigma-Aldrich) was the ionomer used. The mixture of isopropanol and MilliQ water (1:4, wt:wt) was the solvent of the suspension. In order to have the suspension, the mixture of carbon, solvent, and ionomer was sonicated by the ultrasonic horn (Vibra-Cell Ultrasonic Processor VCX 500, Sonics and Materials, Inc.) for 30 seconds at 35% amplitude power. The ice bath was used to cool the mixture. The 7 μL drop of the suspension was deposited onto glassy carbon disk electrodes (GCDE) before drying.

For the Pt-CDC electrodes, the platinum loading was 18 μg cm^{-2}, *I/C* (wt / wt) ratio was 0.5. The same ionomer and solvent were used as in the case of carbon electrodes. Similarly, the mixture was sonicated by the ultrasonic horn with ice for 30 seconds at 35% amplitude power. The 7 μL drop of the suspension was deposited onto GCDE before drying.

3.1.4. Electrochemical cell and cleaning protocol

In electrochemical measurements, cleanliness of glassware and apparatus are of concern. In this study, it was secured by the cleaning protocol. All glassware and apparatus such as platinum electrodes, the measuring cell and components were soaked in hot (80 °C) concentrated sulfuric acid solution (conc. 95−97%, Sigma−Aldrich, puriss. p.a, ACS reagent) with a few drops of hydrogen peroxides (conc. 30%wt, Perhydrol®, the product of Merck) until cooling down to

the room temperature. Then, the glassware was washed with demineralised water to eliminate all acid residues, and finally three times with Milli-Q water (18.2 MΩ cm at 25 °C, and 2 ppb total organic carbon). In this study, all other glassware (pipets, flasks, etc.) were cleaned using the same protocol. The measuring cell was filled with Milli-Q water after the wash to avoid contaminants from the air. The rotator and connectivity components of the RDE device were cleaned with 99.5% ethanol (200 proof, anhydrous, Sigma-Aldrich) solution. The cleaning of the RDE equipment was performed after one or two measurements. This interval cleaning ensured that there was no measurable influence from the impurities after long measuring process.

The measurement cell contains several components. Luggin capillary, which is a glassy component, is present in the **Fig** 3a. The tip of the long capillary was placed close to the working electrode surface to reduce the resistance of electrolyte between the working electrode and a reference electrode. The counter electrode consists of the bridge tube with a permeable membrane at one end to avoid the mixing of the solutions in the main compartment and counter

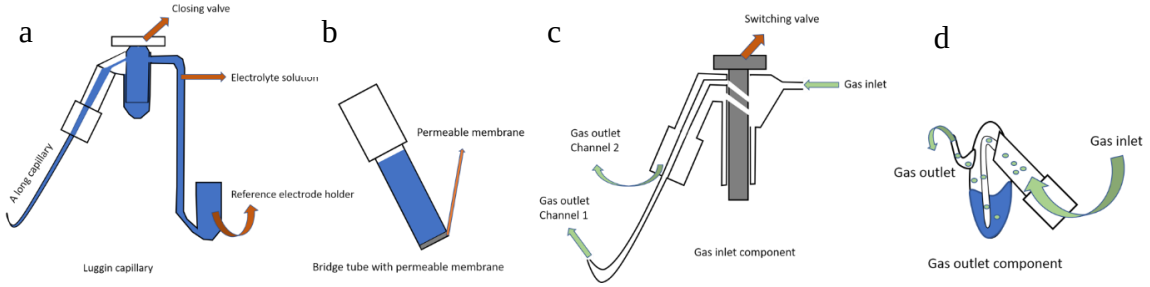

Figure 4. Luggin capillary(a), bridge tube with the permeable membrane (b), gas inlet (c), and gas outlet (d).

electrode compartment (**Fig** 3b). Gas inlet component has a long capillary to let the gas inside or over the solution of measurement cell (**Fig** 3c). The valve of the gas inlet component enables the switchover. Gas outlet component, i.e. water trap, is designed with a small water chamber which isolates the measuring environment and allows the gas to travel only in one direction from inside to the outside (**Fig** 3d). The whole measuring cell assembly is shown in **Fig** 4.

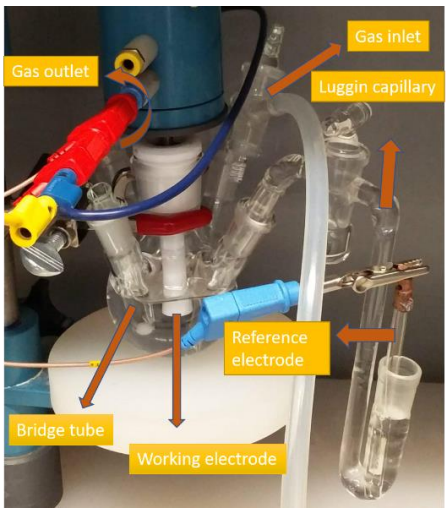

Figure 3. The cell for electrochemical measurements with component assembly.

The electrolyte in electrochemical experiments was 0.1 M $HClO_4$, which was prepared from 70% $HClO_4$ (99,999%, redistilled, Sigma-Aldrich) and Milli-Q water.

3.1.5. Preparation of electrodes

Glassy carbon disk electrodes (GCDE), i.e. working electrodes, were polished with 0.05 μm water-based alumina suspension (Buehler, Inc.) by a figure-eight polishing motion. Polished electrodes were rinsed with Milli-Q water before and after sonicating in an ultrasonic bath for 30 seconds. Electrodes were dried before the catalyst ink was deposited onto a GCDE surface.

In this study, the catalyst was deposited onto GCDE using three depositing/drying techniques. The catalyst suspension was dropped on GCDE and left to dry. Electrodes were dried in atmospheric conditions, called air-drying technique. In isopropanol vapour drying, electrodes were dried slowly in isopropanol vapour at 40 °C. In the last technique, the electrode was mounted to an inverted rotator, which rotates slowly (less than 100 rev min^{-1}) at first. Then the rotating speed was increased to the desired velocity after a drop of catalyst ink was deposited onto the electrode. The deposition technique was optimised until uniform coverage was achieved.

Dynamic hydrogen electrode was prepared in galvanostatic conditions (current of the platinum cathode was −30 mA). Before filling the electrode with 0.1 M $HClO_4$ electrolyte solution, it was saturated with H_2 gas (>99.9999%, Model NMH_2 500, Linde Gas). The anode was a large surface (> 10 cm^2) Pt bar. All the potentials are reference against this electrode, and the electrode is noted as RHE, i.e. reversible hydrogen electrode in solution under study.

The auxiliary electrode was high surface area platinum mesh.

3.2. Electrochemical measurements

Cyclic voltammetry (CV), RDE and electrochemical impedance spectroscopy (EIS) methods were used to characterise the catalyst supports and catalysts. All the electrochemical measurements were performed with potentiostat Metrohm Autolab PGSTAT204.

The cyclic voltammetry was measured in the range of potentials from −0.4 V to 1.1 V vs RHE for carbons and from 0.02 V to1 V vs RHE for the platinum catalyst. In case of carbon, the potential sweep rates were 5, 10, 20, 30, 50, 70, 100, 150, 200, 300, 500, and 1000 mV s^{-1}, but in case of platinum, an additional set of measurement, in which potential sweep rates were 10, 20, 30, 70, 100, 150, 200, 300, and 400 mV s^{-1}, was applied. Both materials were measured in quiescent conditions.

RDE was performed at 10 mV s^{-1} and the rotation speeds were 3000, 2500, 2000, 1500, 1000, 500 and 0 rev min^{-1}. The activity of platinum catalysts was also screened by the technique

suggested by Shinozaki et al. [82], i.e. quick screening measurements at 1600 rev min^{-1} were performed.

The background current measured in the solution saturated with argon (99.9999%, Linde Gas AGA) was subtracted from the current measured in oxygen (99.999%, AGA – the Linde Group AGA) to elucidate the oxygen reduction.

The EIS method was mainly used to establish the solution resistance, R_{el}, between the working electrode and the tip of the Luggin capillary. The EIS was done at 0.8 V vs RHE (ΔE = 10 mV_{rms}, 0.1 Hz $\leq f \leq$ 10 000 Hz, 50 points in logarithmic scale). The potential was corrected during the CV and RDE measurements for *IR*-drop.

The electrochemical experiments were performed at 22±1 °C in the Faraday cage. At least three separate measurements were performed with each material, and the data was averaged. Error bars in figures represent the standard deviation of average.

3.3. Physical characterisation

The porosity of the catalysts was estimated using the low-temperature (−195.8 °C) nitrogen sorption method [88] with a 3FLEX instrument (Micromeritics, USA). A nonlocal density functional theory model "Carbon-N2-77, 2D-NLDFT Heterogeneous surface" [89], available in SAIEUS software [90], (v2.02, Micromeritics, USA) was used to calculate the pore size distribution data. The specific surface area, S_{BET}, values were calculated according to the Brunauer-Emmett-Teller multipoint (BET) theory within the relative pressure range from 0.05 to 0.2. The total volume of pores, V_{tot}, was calculated from the amount of gas adsorbed near the saturation pressure. The *t*-plot method was used to calculate the volume of micropores, V_{micro}.

A Bruker D8 Advance diffractometer with Ni-filtered Cu K_α radiation (0.6 mm wide parallel beam, two 2.5° Soller slits and LynxEye line detector system) was used to measure diffractograms of materials under study. The scanning step of 0.01° for 2θ was applied from 10° to 90°. The total counting time per step was 166 s.

Thermogravimetric analysis (TGA) of the platinum catalysts was performed using a NETZSCH STA449F3 instrument to find out the platinum content in the samples. The temperature range was from 25°C up to 1000 °C, the heating rate was 10 K min^{-1}, and the gas flow rate of synthetic air (20 vol% N_2 and 80 vol% O_2) was 50 cm^3 min^{-1}. Weight of the sample was 10 mg, and an Al_2O_3 pan was used. The purity of nitrogen was 99.999% (AGA - A member of the Linde Group).

4. RESULTS AND DISCUSSION

4.1. Physical characterisation

4.1.1. Low-temperature nitrogen absorption/desorption measurements

C(Cr_3C_2, 800 °C) showed the highest specific surface area amongst studied CDCs. The S_{BET} value was even 8.5 times higher compared to the same material in the previous study [73], and 7.4 times higher than for C(Cr_3C_2, 1000 °C) (**Table** 1). In this study the chlorination of the carbide was made very slowly to ensure the completeness of the reaction and as there was enough time for chlorides to diffuse out of the structure the initial structure of the carbide was retained and not destroyed during the synthesis process. Therefore in material C(Cr_3C_2, 800 °C) highly microporous structure was formed with S_{micro}/S_{BET} = 0.98. Other carbons synthesised were micro-mesoporous. It is believed that at higher temperatures during the long reduction with hydrogen, the surface of materials become more graphitised.

Micropores of all CDCs are distributed around 1 nm (**Fig**. 5 (a)). However, the mesopores of C(Cr_3C_2, 800 °C) are distributed at lower pore widths compared to other CDCs. In detail, mesopores for C(Cr_3C_2, 800 °C) were around 2-3 nm and for others CDCs around 8-10 nm. After deposition of the Pt nanoparticles onto CDCs, the specific surface areas of catalyst materials decreased. The change indicated the modification of the structure of carbon support.

***Table** 1*. Low-temperature nitrogen adsorption/desorption measurement results for the catalyst supports C(Cr_3C_2) and the catalysts Pt-C(Cr_3C_2).

Material/ Parameter	S_{BET} / $m^2 g^{-1}$	S_{micro} / $m^2 g^{-1}$	S_{meso} / $m^2 g^{-1}$	S_{micro}/S_{BET}	V_{tot} / $cm^3 g^{-1}$	V_{micro} / $cm^3 g^{-1}$	V_{meso} / $cm^3 g^{-1}$
C(Cr_3C_2, 800 °C)	2287	2233	55	0.98	1.14	1.14	0
C(Cr_3C_2, 900 °C)	238	42	196	0.18	0.39	0.02	0.37
C(Cr_3C_2, 1000 °C)	311	78	233	0.25	0.65	0.03	0.62
C(Cr_3C_2, 1100 °C)	252	77	175	0.30	0.72	0.03	0.69
Pt-C(Cr_3C_2, 800 °C) UIGR	385	100	285	0.35	0.30	0.04	0.26
Pt-C(Cr_3C_2, 800 °C) MWEG	410	54	356	0.13	0.29	0.02	0.27
Pt-C(Cr_3C_2, 900 °C) MWEG	130	10	120	0.08	0.20	0.002	0.20
Pt-C(Cr_3C_2, 1000 °C) MWEG	210	30	180	0.14	0.44	0.01	0.44
S_{BET} – specific surface area, S_{micro} – micropore area, S_{meso} – mesopore area, V_{tot} – total pore volume, V_{micro} – micropore volume, V_{meso} – mesopore volume							

Furthermore, the decrease was more pronounced in the case of C(Cr_3C_2, 800 °C) - it is 5-6 times in case of both synthesis methods. There were differences between Pt-C(Cr_3C_2, 800 °C) UIGR and Pt-C(Cr_3C_2, 800 °C) MWEG in areas of micro- and mesopores, i.e. the difference in S_{micro}/S_{BET} is about three times, however, S_{BET}, V_{tot}, V_{micro} and V_{meso} were practically the same (**Table** 1). These two materials were even similar to each other in pore-width distribution (**Fig**. 5 (b)). Both materials have two-peak distribution, in which the dominant pore size was from 0.35 to around 1 nm, the second peak is in the area of mesopores from 2 to 10 nm (**Fig**. 5 (b)). Both materials have mesopores, which are desirable for optimal catalyst activity. Unfortunately, the catalyst Pt-C(Cr_3C_2, 800 °C) UIGR presented low ORR activity –discussed later.

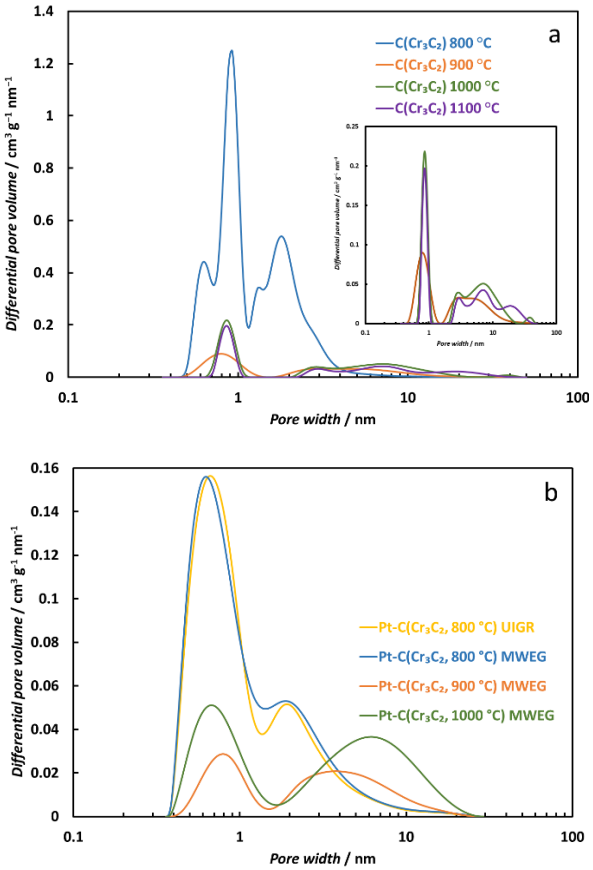

Figure 5. Pore-width distributions (a) for the catalyst support C(Cr_3C_2) and (b) for the catalysts Pt-C(Cr_3C_2).

Although Pt-C(Cr_3C_2, 900 °C) MWEG and Pt-C(Cr_3C_2, 1000 °C) MWEG were also two-peak distributions, micropores from 0.35 to 1 nm were not dominant in their structure. The ratio of micropores to mesopores is not very different for all catalysts Pt-C(Cr_3C_2). However, the mesopores distribution of these catalysts is slightly different. Mesopore distribution is broader for materials for Pt-C(Cr_3C_2, 900 °C) with a maximum around 4 nm, and for Pt-C(Cr_3C_2, 1000 °C) with a maximum around 8 nm (**Fig**. 5b). This difference could be caused by the structure of carbon support C(Cr_3C_2) (**Fig**. 5a).

4.1.2. X-Ray diffraction (XRD)

The diffractograms in **Fig**. 6 (a) confirm that all C(Cr_3C_2) do not contain precursor Cr_3C_2, because of there no visible peaks in the diffractograms of CDC corresponding to the precursor. The crystallinity of CDCs increase with synthesised temperature because the peaks become sharper, i.e. the crystallite size of carbon increases.

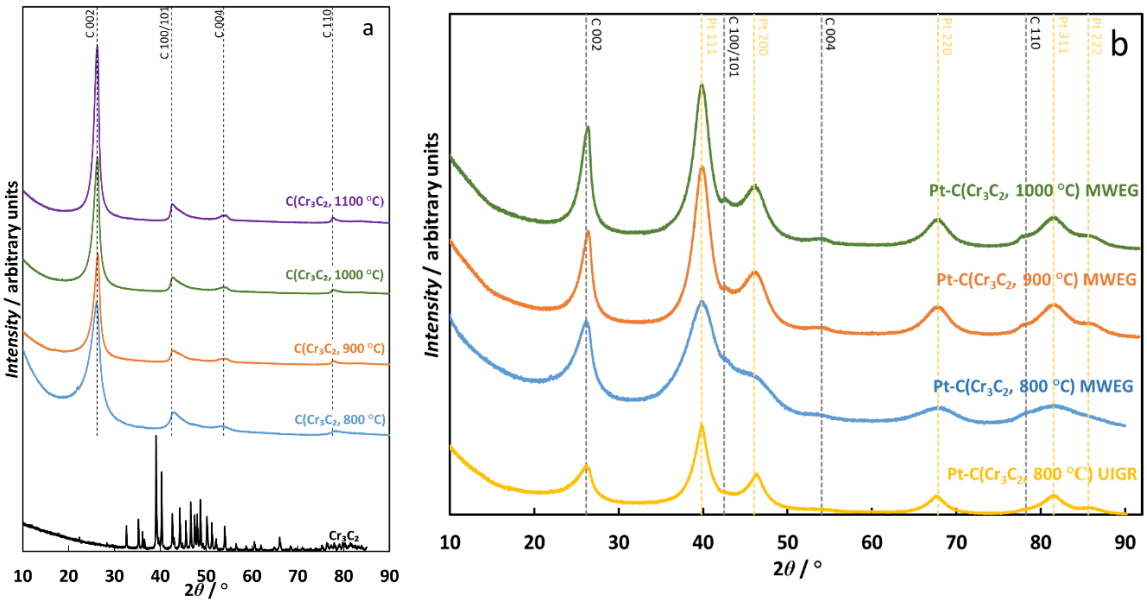

Figure 6. Diffractograms (a) for the catalyst supports C(Cr_3C_2) and precursor Cr_3C_2, and (b) for the catalysts Pt- C(Cr_3C_2).

The diffractograms of platinum catalysts are given in **Fig** 6 (b). The presence of Pt peaks indicated the successful deposition. The Pt peaks of Pt-C(Cr_3C_2, 800 °C) UIGR were slightly sharper compared to the material synthesised with the MWEG method. It could indicate that the material Pt-C(Cr_3C_2, 800 °C) UIGR might have bimodal or even multimodal distribution of platinum crystallites sizes.

The crystallite size, *d*, could be estimated from Scherrer equation [91]:

$$d = \frac{K\lambda}{\beta \cos\theta} \qquad \textbf{(Eq. 34)}$$

where K is a dimensionless shape factor (K = 0.93), λ is the characteristic wavelength, θ is the Bragg angle, and β is the full width at half maximum of reflections. According to the XRD results, the average size of platinum crystallites was from 2-3.3 nm (**Table** 2).

Table 2. Summary of electrochemical measurements for the catalysts Pt-C(Cr_3C_2) and the crystallite sizes of platinum nanoparticles.

Material / Parameter	**wt% of Pt**	***ECA* / $m^2\ g^{-1}$**	**d_{ECA} / nm**	**d_{XRD} / nm**	***MA* / $A\ g^{-1}_{Pt}$**	***SA* / $A\ m^{-2}_{Pt}$**	***n***
Pt-C(Cr_3C_2, 800 °C) UIGR	19	24 ± 7	12.8 ± 3.8	2.0	21.5 ± 5.7	0.9 ± 0.1	1.3 ± 0.1
Pt-C(Cr_3C_2, 800 °C) MWEG	19	34 ± 2	8.5 ± 0.7	2.2	95 ± 15	2.8 ± 0.4	3.4 ± 0.1
Pt-C(Cr_3C_2, 900 °C) MWEG	22	21 ± 2	13 ± 1	3.2	60 ± 15	2.8 ± 0.5	3.6 ± 0.2
Pt-C(Cr_3C_2, 1000 °C) MWEG	22	27 ± 2	10.3 ± 0.7	3.3	59 ± 12	2.2 ± 0.5	3.2 ± 0.1
ECA – electrochemical activity, d_{ECA} – diameter of Pt particles calculated from ECA, d_{XRD} – diameter of Pt crystallites calculated from XRD, *MA* – mass activity, *SA* – specific activity, *n* – number of transferred electron							

4.1.3. Thermogravimetric analysis

TGA was performed to find out the content of platinum in catalysts and elucidate the thermal stability of the catalysts. During the controlled temperature increase, the carbon is oxidised step-by-step in synthetic air (**Fig.** 7). The content of platinum in all samples was around 20 wt% and is given in **Table** 8. The catalysts start to decompose at 400 °C, and the decomposition is complete at 650 °C. For catalyst Pt-C(Cr_3C_2, 800 °C) which has most porous and amorphous carbon support the curve is shifted about 50 °C compared to catalysts Pt-C(Cr_3C_2, 900 °C) and Pt-C(Cr_3C_2, 1000 °C). The synthesis method did not influence the thermogravimetric curve of the catalyst Pt-C(Cr3C2, 800 °C) noticeably.

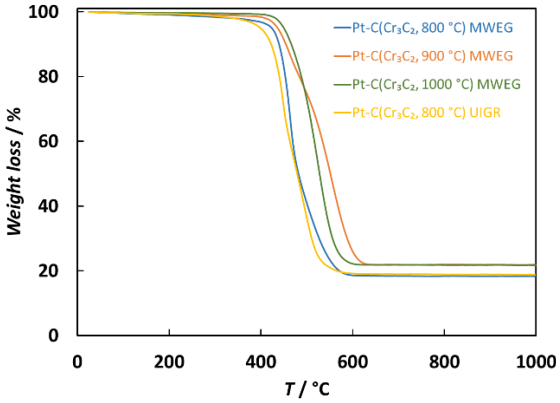

Figure 7. Thermogravimetric curves of the catalysts Pt-C(Cr_3C_2) in synthetic air (20 vol% N_2 and 80 vol% O_2). The temperature was increased at 10 K min^{-1}, and the gas flow rate was 50 cm^3 min^{-1}.

4.2. Electrochemical measurements

4.2.1. Capacitive behaviour of catalyst supports and catalysts

The CV was used to characterise the capacitive behaviour of synthesised materials in 0.1M $HClO_4$ solution saturated with argon. The current density, j (A m^{-2}), was calculated from the current, I (A), by the equation, **Eq**. 35 below:

$$j = \frac{I}{S}, \qquad \text{(Eq. 35)}$$

where S (m^2) is the geometric area of the electrode surface area. The sample voltammograms for materials C(Cr_3C_2, 900 °C) and Pt-C(Cr_3C_2, 900 °C) MWEG are given in **Fig.** 8. The current density is proportional to the potential sweep rate. This is characteristic to capacitive process, i.e. reversible adsorption/desorption on the electrode surface. The cyclic voltammograms of C(Cr_3C_2) are relatively featureless at high potential sweep rates (**Fig.** 8a). However, there are three distinct regions in the cyclic voltammograms of Pt-C(Cr_3C_2) (**Fig.** 8b). At electrode potentials less than 0.35 V, there are two developed symmetric peaks, which are caused by the reversible hydrogen adsorption and desorption on the surface of platinum nanoparticles [92]. At potentials more positive than 0.7 V, the oxygen adsorption takes place. The middle section 0.4 V < E < 0.6 V is a so-called electrical double (EDL) layer region.

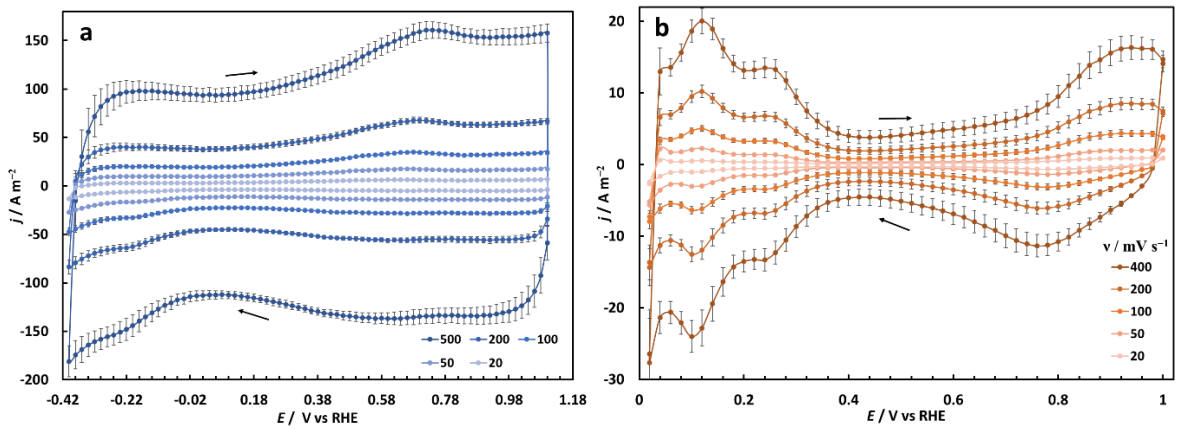

Figure 8. Dependence of current density, *j*, on electrode potential, *E*, at different potential sweep rates, *v*, in Ar saturated 0.1 M $HClO_4$ electrolyte for (a) catalyst support C(Cr_3C_2, 900 °C) and (b) catalyst Pt-C(Cr_3C_2, 900 °C) MWEG.

In order to study the capacitive response of materials and to have better visualisation behaviour of cyclic voltammograms at lower sweep rates, the measured currents from CV were converted into gravimetric capacitance, *C* (F g^{-1}), by the equation:

$$C = \frac{I}{vm} \qquad \text{(Eq. 36)}$$

where *I* (A) is the measured current, *v* (V s^{-1}) is the potential sweep rate, and *m* (g) is a mass of catalyst support or platinum catalyst (without Nafion) on GCDE. The *CE*-curves for materials C(Cr_3C_2, 1000 °C) and Pt-C(Cr_3C_2, 1000 °C) are presented in **Fig.** 9. In case of catalyst supports C(Cr_3C_2) at lower sweep rates, there is a noticeable increase of current density |*j*| at potentials more negative than 0 V which is probably caused by the hydrogen evolution on the carbon surface (**Fig.** 9a). The onset of the carbon oxidation could be the cause of the slight increase of current density at potentials more positive than 1.0 V. As these processes are very slow, they do not influence the shape of cyclic voltammograms at higher sweep rates. On the other hand, the cyclic voltammograms of the Pt-C(Cr_3C_2) catalysts (**Fig.** 9b) lye nicely on each

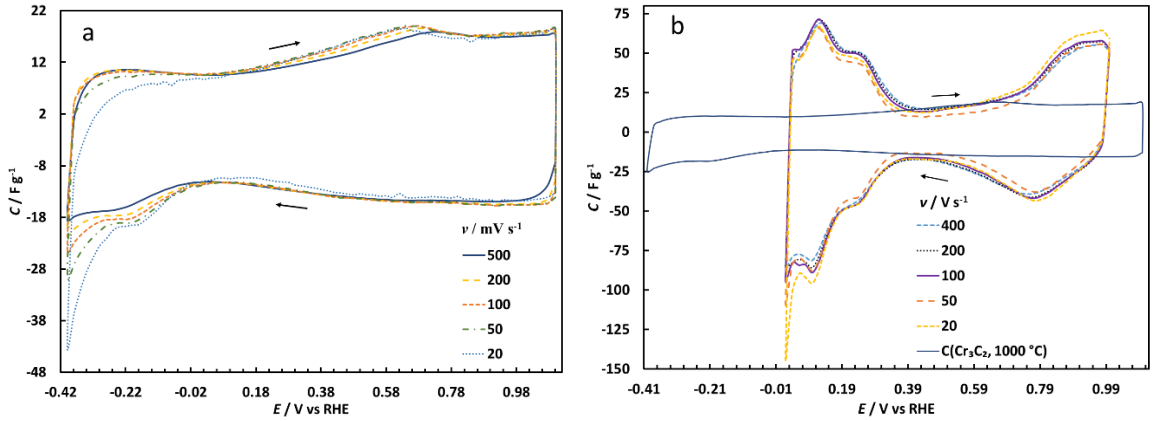

Figure 9. Dependence of capacitance, *C*, on electrode potential, *E*, at different potential sweep rates, *v*, in Ar saturated 0.1 M $HClO_4$ electrolyte for (a) catalyst support C(Cr_3C_2, 1000 °C) and (b) catalyst Pt-C(Cr_3C_2, 1000 °C) MWEG.

other. This indicates that the adsorption/desorption processes are reversible, and there are no contaminants in the solution because the region of hydrogen adsorption/desorption is very sensitive to all sorts of impurities.

The *CE*-curves for catalyst supports and catalysts at constant sweep rate 100 mV s^{-1} are demonstrated in **Fig.** 10. The materials C(Cr_3C_2, 900 °C) and C(Cr_3C_2, 1000 °C) exhibit very similar capacitance (**Fig.** 10a) as they also have close specific surface area values (**Table** 1). However the capacitance of C(Cr_3C_2, 800 °C), 93 F g^{-1} was ca. six times higher than for C(Cr_3C_2, 900 °C) and C(Cr_3C_2, 1000 °C), which was 16 F g^{-1} for both materials. This observation is following the trends in specific surface area measurements of catalyst supports C(Cr_3C_2) (**Table** 1). The material C(Cr_3C_2, 800 °C) can be used as the electrode material for the electric double layer capacitor. The deposition of platinum particles onto carbon support

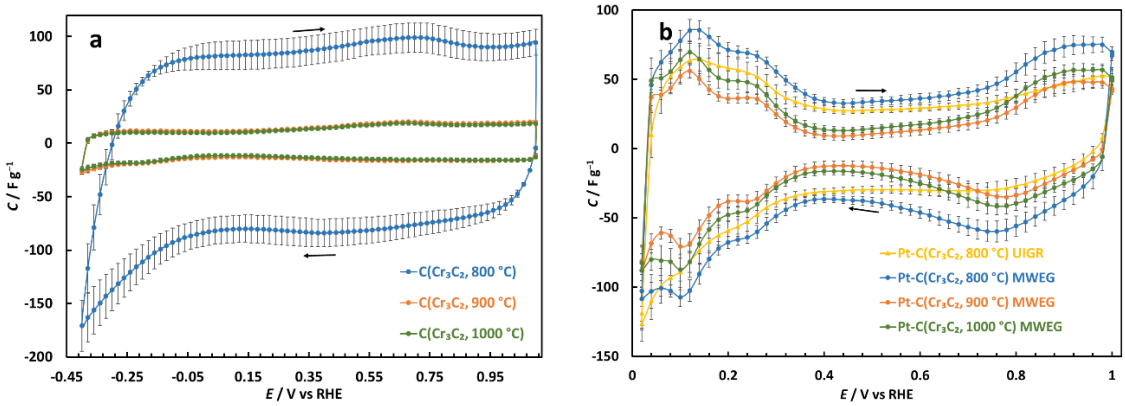

Figure 10. Dependence of capacitance, *C*, on electrode potential, *E*, at 100 mV s^{-1} in Ar saturated 0.1 M $HClO_4$ electrolyte for (a) catalyst supports C(Cr_3C_2) and (b) catalysts Pt-C(Cr_3C_2).

C(Cr_3C_2, 800 °C) caused a substantial decrease of capacitance (**Fig.** 10a). This decrease is in agreement with the decrease of the specific surface area of catalyst Pt-C(Cr_3C_2, 800 °C). However, this is not caused only by the 20% reduction of carbon in the catalyst. Probably also some of the micropores are blocked with platinum nanoparticles as could be deduced by the drastic change of the S_{micro}/S_{BET} ratio (**Table** 1) and from the pore size distribution (**Fig.** 5). In the region of hydrogen adsorption/desorption, the capacitance depends directly on the dispersion of platinum nanoparticles.

From the region of hydrogen adsorption/desorption, the active surface area of platinum nanoparticles or active electrochemical area (ECA) could be estimated using the equation [93]:

$$ECA = \frac{Q_H}{m_{Pt} Q_{H\ ref}} \qquad \text{(Eq. 37)}$$

where $Q_{H\ ref}$ is the reference charge value of formation Pt-H on the smooth polycrystalline platinum (0.21 mC cm^{-2}) [94], m_{Pt} (g) is the mass of platinum on the electrode and Q_H (C g^{-1})

is the total charge needed to adsorb monolayer of hydrogen atoms on the platinum surface. In detail, Q_{H} was calculated by the following equation [78]:

$$Q_{\mathrm{H}} = 0.5 \times (Q_{\mathrm{total}} - Q_{\mathrm{EDL}}) \quad \textbf{(Eq. 38)}$$

where Q_{total} (C g^{-1}) and Q_{EDL} (C g^{-1}) are the total charge and the charge of EDL, respectively, which were obtained in the potential region of hydrogen adsorption/desorption. In addition, the diameter of Pt nanoparticles, d_{ECA} (nm), can be estimated from the ECA value [26].

$$d_{\mathrm{ECA}} = \frac{6}{\rho_{\mathrm{Pt}} ECA \times 10^9} \quad \textbf{(Eq. 39)}$$

where $\rho_{\mathrm{Pt}} = 21.45 \times 10^6$ (g m^{-3}) is the density of platinum [95]. It was assumed that the platinum nanoparticles are spherical. Nevertheless, this kind of diameter estimation is strongly affected by the dispersion of Pt nanoparticles on the support surface.

The *ECA* and d_{ECA} values are given in **Table** 2. The ECA value decreases in the order of catalysts Pt-C(Cr_3C_2, 800 °C) MWEG > Pt-C(Cr_3C_2, 1000 °C) MWEG > Pt-C(Cr_3C_2, 800 °C) UIGR > Pt-C(Cr_3C_2, 900 °C) MWEG. In the same order, the diameter of platinum nanoparticles increases. The diameter of the crystallites calculated from the XRD data is several times lower compared to particle size dimensions calculated from the cyclic voltammetry data. Probably one platinum nanoparticle consists of several crystallites, and this reduces the d_{ECA} value. Part of the 1-2 nm size platinum nanoparticles might be deposited into narrow micropores of carbon support and are inaccessible to electrolyte and therefore "invisible" to electrochemistry. Also, the carbon support and deposition method influence the particle size of platinum nanoparticles.

4.2.2. Oxygen reduction reaction

4.2.2.1. Cyclic voltammetry

ORR on all materials synthesised was studied in 0.1 M $HClO_4$ solution. The current densities measured in the oxygen-saturated solution, j_{O_2}, were corrected for the current densities measured in argon- saturated solution, j_{Ar}:

$$j_{\mathrm{c}} = j_{O_2} - j_{\mathrm{Ar}} \quad \textbf{(Eq. 40)}$$

to obtain the corrected current densities corresponding to ORR, i.e. current densities were corrected for EDL charging effects.

The cyclic voltammograms for catalyst supports C(Cr_3C_2) and catalysts Pt-C(Cr_3C_2) for ORR are shown in **Fig.** 11. The ORR on catalyst supports C(Cr_3C_2) proceeds in two steps. In the first step, the hydrogen peroxide is formed. This behaviour was consistent with the

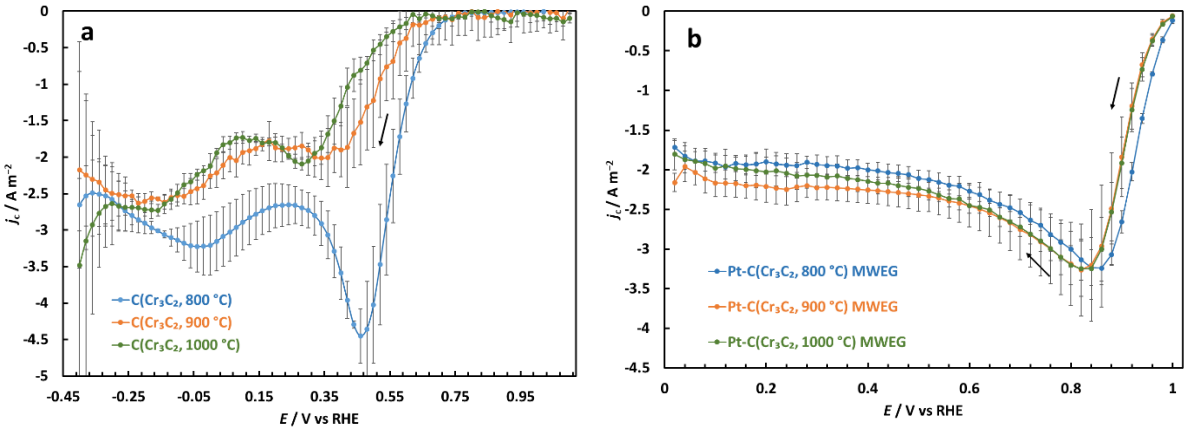

Figure 11. Oxygen reduction current densities, j_c, vs electrode potential, E, in 0.1 M $HClO_4$ solution saturated with oxygen at potential sweep rate 10 mV s^{-1} for (a) catalyst supports C(Cr_3C_2) and (b) catalysts Pt-C(Cr_3C_2).

2-electron process of glassy carbon [42]. However, there is a very distinct second peak at negative potentials, which corresponds to the reduction of hydrogen peroxide to water. Material C(Cr_3C_2, 800 °C) have the lowest overpotential among catalyst supports (**Fig.** 11a). C(Cr_3C_2, 900 °C) and C(Cr_3C_2, 1000 °C) exhibited lower activity towards ORR. Furthermore, C(Cr_3C_2, 800 °C) presents higher current density $|j_c|$ as the first peak is about 2.5 A m^{-2} higher. As expected, the catalysts Pt-C(Cr_3C_2) have much higher activity. The most active catalyst is Pt-C(Cr_3C_2, 800 °C), whose overpotential is 20 mV lower compared to other platinum catalysts (**Fig.** 11b). There is only one peak on the cyclic voltammogram corresponding to the 4-electron ORR process (or to the 2+2 process). There is no anodic peak on cyclic voltammograms, i.e. the ORR was irreversible process on these materials.

The dependence of the first peak potential, E_p, on the potential sweep rate in 0.1 M $HClO_4$ solution saturated with oxygen for catalyst supports C(Cr_3C_2) and catalysts Pt-C(Cr_3C_2) is shown in **Fig.** 12. As the potential sweep rate increases, the peaks shift towards more negative potentials. The irreversible ORR causes this shift. The E_p vs ln v

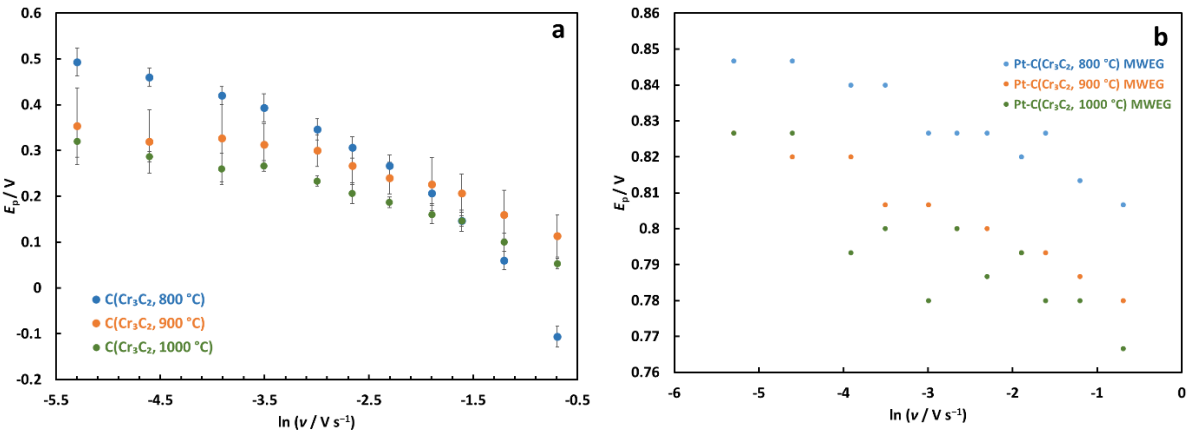

Figure 12. The dependence of the first peak potential, E_p, on potential sweep rate, ln v, in 0.1 M $HClO_4$ solution saturated with oxygen for (a) catalyst supports C(Cr_3C_2) and b) catalysts Pt-C(Cr_3C_2).

dependencies is linear for platinum catalysts. However, they are curved for carbon supports. These curves could be caused by the mass transport limitations in the thick layer of the catalyst support on the electrode. Therefore, models developed for flat surfaces could not be applied straightforwardly.

The dependence of the first peak current density, j_p, on potential sweep rate, $v^{½}$, is linear for studied materials **(Fig. 13)**. This dependence indicates the diffusion limitation of ORR. The slope values are similar for platinum catalysts, i.e. mass transport conditions within the catalyst layer are alike. However, the slopes are somewhat different for catalyst supports. The difference demonstrates that slightly different mass transport conditions are realised in a thick layer of catalyst supports. At higher sweep rates, the difference is even more pronounced. The intercepts as well are not equal to zero, which could indicate mass transport limitations inside the catalyst layer.

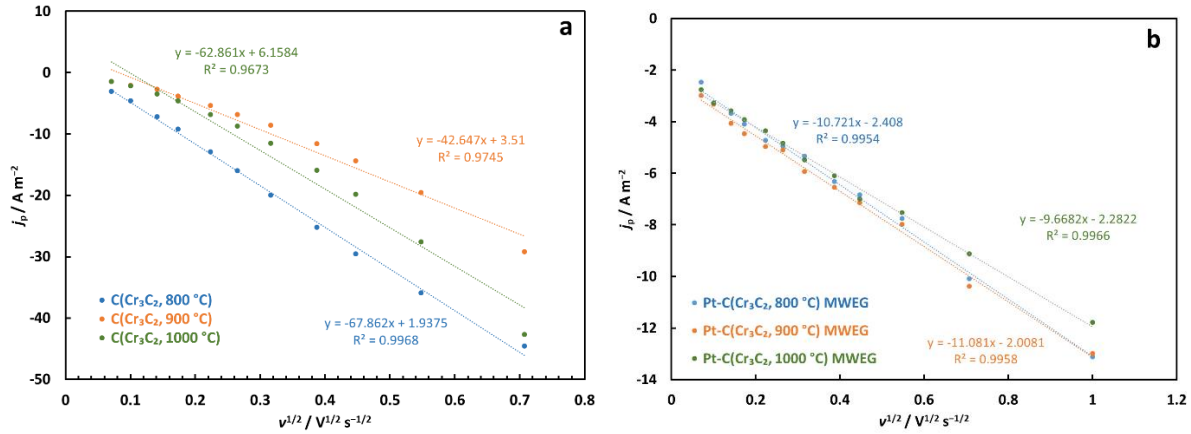

Figure 13. The dependence of the first peak current density, j_p, on potential sweep rate, $v^{½}$, in 0.1 M $HClO_4$ solution saturated with oxygen for (a) catalyst supports $C(Cr_3C_2)$ and b) catalysts $Pt\text{-}C(Cr_3C_2)$.

4.2.2.2. Rotating disc electrode method

The rotating disc electrode method was used to study in more detail the ORR mechanism and calculate the kinetic current density of ORR. The j_c vs E dependences at different electrode rotations speeds for catalyst support $C(Cr_3C_2, 800\ °C)$ and catalyst $Pt\text{-}C(Cr_3C_2, 800\ °C)$ MWEG are given in **Fig**. 14. The j_c,E-curve could be divided into three regions. These sections are considered using $Pt\text{-}C(Cr_3C_2, 800\ °C)$ MWEG as sample (**Fig.** 14b). There is no dependence of ORR current density on the rotation speed of the electrode at potentials more positive than 0.9 V, and here the reaction speed depends only on the charge transfer kinetics, i.e. the kinetics of ORR is so sluggish that the surface concentration of oxygen molecules is equal to the bulk value. The dependence of current density, j_c, on the electrode potential is not very pronounced

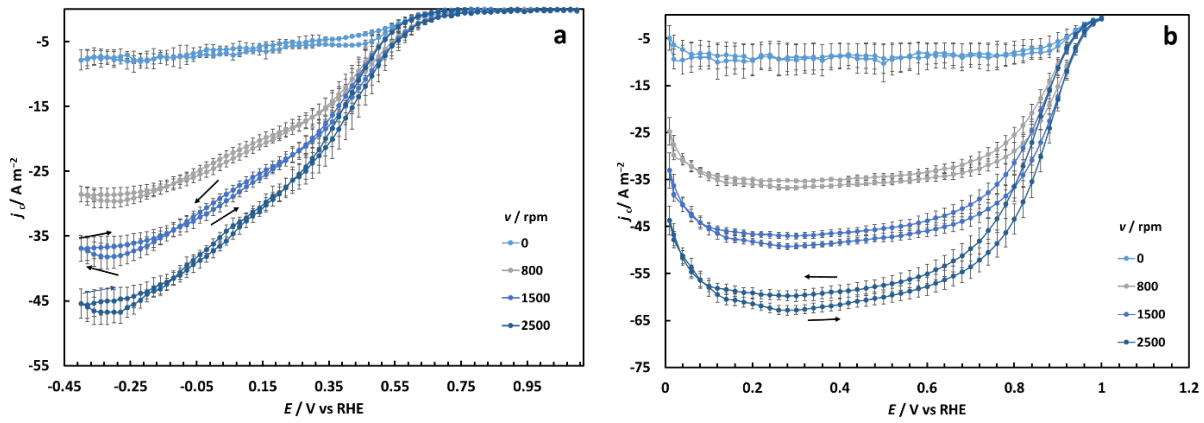

Figure 14. Oxygen reduction current densities, j_c, vs electrode potential, E, in 0.1 M $HClO_4$ solution saturated with oxygen at different rotation speeds for (a) catalyst support C(Cr_3C_2, 800°C) (10 mV s^{-1}) and (b) catalyst Pt-C(Cr_3C_2, 800°C) MWEG (10 mV s^{-1}).

in the potential region from 0.1 V to 0.7 V. However, there is very marked dependence on the rotation speed of the electrode. The electrode kinetics are covered only by mass-transfer in this region, as the ORR overpotential is high enough to support high mass-transfer limited current densities, $|j_d|$. As ORR on the materials under investigation is not reversible, the width of this region depends on the rotation speed. The high mass-transfer limited current densities, $|j_d|$, increase as the rotation speed of the electrode is increased because the thickness of diffusion layer is decreased and the concentration gradient of oxygen at the surface increase. ORR is governed by slow charge transfer, and mass transfer kinetics in the middle section from 0.7 V to 0.9 V. This is the so-called region of mixed kinetics. In case of platinum catalysts, the current density, $|j_c|$, starts to decrease at potentials less positive than 0.1 V, this is caused by the enhanced formation of hydrogen peroxide in the region of hydrogen adsorption and desorption on the platinum electrodes. There is also one other feature characteristic of platinum catalysts. The ORR current densities, $|j_c|$, of the anodic sweep, are always higher in the region of mixed kinetics because ORR takes place on the platinum surface, which is not yet covered with a uniform oxide layer. The same behaviour could also be observed in the case of carbon supports C(Cr_3C_2, 800 °C) (**Fig.** 14a). Although there are not well-defined current plateaus because of the ORR mechanism changes with the potential, i.e. 2-electron mechanism is replaced by 2+2 electron mechanism. As the number of electrons transferred is lower for catalyst support, the current density, $|j_c|$, is also lower.

The rotation disc electrode data of catalyst supports C(Cr_3C_2) and catalysts Pt-C(Cr_3C_2) are compared in **Fig.** 15. The ORR overpotential of catalyst supports C(Cr_3C_2) increases in order C(Cr_3C_2, 800 °C) < C(Cr_3C_2, 900 °C) < C(Cr_3C_2, 1000 °C) (**Fig.** 15a). In the same order increases the graphitisation of the carbons (**Fig.** 6). It could be speculated that as the synthesis

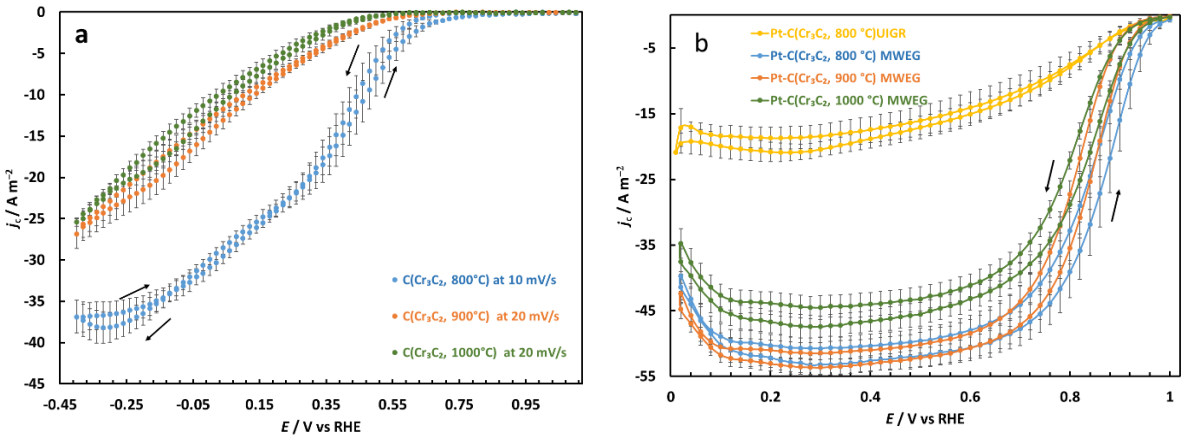

Figure 15. Oxygen reduction current densities, j_c, vs electrode potential, E, in 0.1 M $HClO_4$ solution saturated with oxygen for (a) catalyst supports $C(Cr_3C_2)$ and (b) catalysts Pt-$C(Cr_3C_2)$ (20 mV s^{-1}).

temperature increases the ordering of carbon takes place and the amount of defects in the carbon structure decreases, therefore, the number of active sites for ORR is reduced and the ORR activity decreases. The activity of the material $C(Cr_3C_2$, 800 °C) is remarkably higher. This could also be attributed to much higher specific surface area (**Table** 1), as the kinetic current is proportional to the true surface area. The ORR overpotential of catalyst supports $C(Cr_3C_2)$ increases in order Pt-$C(Cr_3C_2$, 800 °C) MWEG < Pt-$C(Cr_3C_2$, 900 °C) MWEG ≈ Pt-$C(Cr_3C_2$, 1000 °C) MWEG < Pt-$C(Cr_3C_2$, 800 °C) UIGR (**Fig.** 15b). The ORR activity of platinum catalysts synthesised using MWEG methods follows the general trend in ECA (**Table** 2) – the catalyst Pt-$C(Cr_3C_2$, 800 °C) MWEG has the highest ECA and also highest ORR activity. The platinum catalyst synthesised using UIGR is much lower. The reason is unclear. The structure of the catalyst could cause it, i.e. the UIGR method facilities the synthesis of very small (< 2 nm) platinum nanoparticles which could be deposited into micropores and might be not accessible to the electrolyte. The XRD analysis also supports the explanation. Other reason could be connected to the uniformity of the catalyst layer. It was challenging to disperse this catalyst on GCDE. If the catalyst layer is not uniform, then the kinetic behaviour is also compromised. The CV and RDE methods give consistent activity estimation.

The Koutechký-Levich method was used to estimate kinetic current densities, j_k, and the numbers of electrons transferred in ORR, n. The K-L plots at different potentials were linear. From the intercept of the K-L lines, the kinetic current densities were calculated, and the number of electrons transferred in reaction could be found from the slope.

The kinetic current densities are presented as Tafel plots (**Fig.** 16). The general trends in activities for catalyst supports $C(Cr_3C_2)$ and catalysts Pt-$C(Cr_3C_2)$ are also followed in the

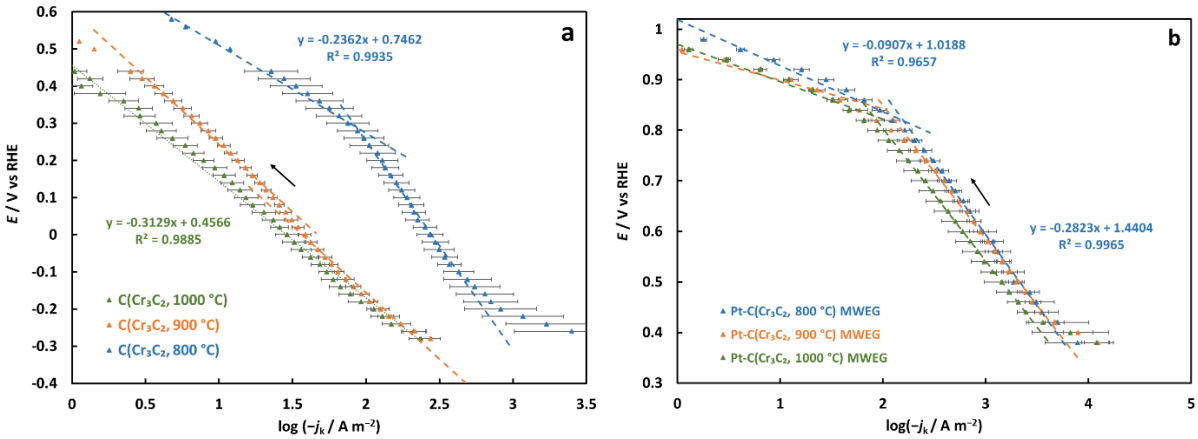

Figure 16. Tafel plot from anodic sweep for (a) catalyst supports $C(Cr_3C_2)$, and (b) catalysts Pt-$C(Cr_3C_2)$ in 0.1 M $HClO_4$ saturated with oxygen.

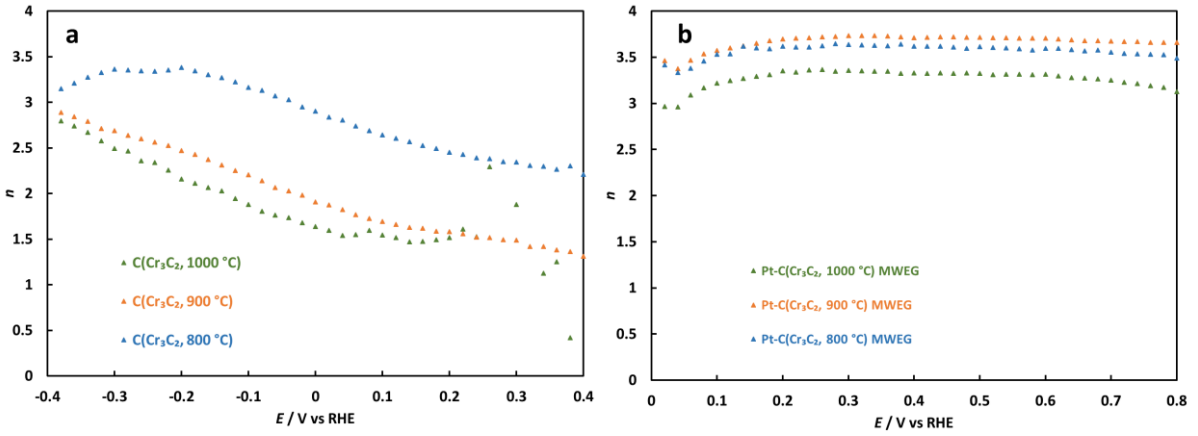

Figure 17. Number of transferred electrons, *n*, from anodic sweep for (a) catalyst supports $C(Cr_3C_2)$, and (b) catalysts Pt-$C(Cr_3C_2)$ in 0.1 M $HClO_4$ saturated with oxygen.

Tafel plot. The slopes of Tafel plots were calculated, and the slopes are shown in the figure. The slope values for carbon supports are very high, more than 200 mV^{-1}. Those slope values could be caused by very thick catalyst layers, which could hinder the calculation of correct kinetic parameters. There are two regions in Tafel plots for platinum-based catalysts, so-called low-current and high current regions. The Tafel slope is 90 mV^{-1} in the low current region, and this is a reasonable value. The very high value of Tafel slope in the high-current region could be influenced by the mass transport difficulties in the catalyst layer.

For platinum catalysts Pt-$C(Cr_3C_2)$, the number of electrons transferred is around 3.5 and does not depend on the electrode potential (**Fig.** 17b). However, it is lower for the material Pt-$C(Cr_3C_2$, 1000 °C) MWEG and much lower for the material Pt-$C(Cr_3C_2$, 800 °C) UIGR. The decrease of *n* value could also be explained by the non-uniformity of the catalyst layer on the GCDE. In the case of catalyst supports $C(Cr_3C_2)$, the number of electrons depends on the

electrode potential and changes from two to three (**Fig.** 17a). This result is in a good agreement with CV data (**Fig.** 11a). The *n* value is highest for the support C(Cr_3C_2).

Mass activity, *MA* (A g^{-1}_{Pt}), and specific activity, *SA* (A m^{-2}), was calculated from the measured current, $I_{0.9\ V}$ (A), at the potential 0.9 V [96].

$$\mathrm{MA} = \frac{I_{0.9\ \mathrm{V}}}{m_{\mathrm{Pt}}} \qquad \textbf{(Eq}.\ 41)$$

$$SA = \frac{MA}{ECA} \qquad \textbf{(Eq}.\ 42)$$

In comparison amongst Pt-CDCs, Pt-C(Cr_3C_2, 800 °C) MWEG and Pt-C(Cr_3C_2, 900 °C) MWEG exhibited the highest *SA* (2.8 A m^{-2}_{Pt}). Pt-C(Cr_3C_2, 800 °C) MWEG has the highest *MA* (95 A g^{-1}_{Pt}).

5. SUMMARY

In this work, carbon supports C(Cr_3C_2) were synthesised from Cr_3C_2 using high-temperature chlorination method at selected temperatures 800, 900, 1000 and 1100°C. The carbon C(Cr_3C_2, 800°C) was microporous with very high specific surface area (2287 $m^2\ g^{-1}$). Other carbons have much lower specific surface area and micro-mesoporous. X-ray diffraction (XRD) revealed that the carbon crystallites increased with the synthesis temperature and synthesised C(Cr_3C_2) did not contain a precursor.

Cyclic voltammetry measurements in 0.1 M $HClO_4$ revealed that C(Cr_3C_2) materials show capacitive behaviour. The capacitance of C(Cr_3C_2, 800°C) was 93 F g^{-1}, and it could be suitable for energy storage application. All carbons materials showed activity towards oxygen reduction (ORR). In cyclic voltammograms, two separated electron transfer processes could be distinguished, i.e. the formation of hydrogen peroxide in the first step and the reduction of hydrogen peroxide to water at more negative potentials. The C(Cr_3C_2, 800°C) material had the highest activity towards ORR amongst carbons.

Two methods were used to deposit the platinum nanoparticles onto the carbon support C(Cr_3C_2, 800°C). Ultrasound-assisted incipient wetness impregnation with hexachloroplatinic acid in ethanol, and further gas phase reduction under hydrogen atmosphere received the desired loading of platinum. However, the ORR activity was low. Ultrasound-microwave-assisted polyol method (MWEG) with hexachloroplatinic acid as the precursor and ethylene glycol as the environment and reducing agent received well-dispersed platinum catalyst with desired ORR activity. The platinum nanoparticles were deposited onto the carbon supports Pt-C(Cr_3C_2, 900°C) and Pt-C(Cr_3C_2, 1000°C) using MWEG method. The platinum loading (20-weight percent) was confirmed by thermogravimetry. XRD confirmed the presence of platinum nanoparticles with crystallite sizes from 2.2 nm to 3.3 nm. The materials Pt-C(Cr_3C_2) had a micro-mesoporous structure with the specific surface area from 130 $m^2\ g^{-1}$ to 410 $m^2\ g^{-1}$. The material Pt-C(Cr_3C_2, 800°C) had the lowest ORR overvoltage; and highest mass activity (95 A $g^{-1}{}_{Pt}$) and electrochemically active area (34 ± 2 $m^2\ g_{Pt}{}^{-1}$).

6. REFERENCES

[1] U. Lucia, Overview on fuel cells, *Renew. Sustain. Energy Rev.* 30 (2014) 164–169.

[2] T. Maiyalagan, S. Pasupathi, Components for PEM Fuel Cells: An Overview, *Mater. Sci. Forum.* (2010).

[3] Y. Wang, K.S. Chen, J. Mishler, S.C. Cho, X.C. Adroher, A review of polymer electrolyte membrane fuel cells: Technology, applications, and needs on fundamental research, *Appl. Energy.* 88 (2011) 981–1007.

[4] Y.-L. Ma, J.S. Wainright, M.H. Litt, R.F. Savinell, Conductivity of PBI Membranes for High-Temperature Polymer Electrolyte Fuel Cells, *J. Electrochem. Soc.* 151 (2004) A8–A16.

[5] K. Jiao, X. Li, Water transport in polymer electrolyte membrane fuel cells, *Prog. Energy Combust. Sci.* 37 (2011) 221–291.

[6] N.A. Vante, H. Tributsch, Energy conversion catalysis using semiconducting transition metal cluster compounds, *Nature* 323 (1986) 431.

[7] J.L. Fernández, V. Raghuveer, A. Manthiram, A.J. Bard, Pd-Ti and Pd-Co-Au electrocatalysts as a replacement for platinum for oxygen reduction in proton exchange membrane fuel cells, *J. Am. Chem. Soc.* 127 (2005) 13100–13101.

[8] R. Bashyam, P. Zelenay, A class of non-precious metal composite catalysts for fuel cells, *Nature* 443 (2006) 63–66.

[9] S. Samad, K.S. Loh, W.Y. Wong, T.K. Lee, J. Sunarso, S.T. Chong, W.R. Wan Daud, Carbon and non-carbon support materials for platinum-based catalysts in fuel cells, *Int. J. Hydrog. Energy* 43 (2018) 7823–7854.

[10] V. Swope, I. Sasaki, A. Ay, G.M. Swain, Conductive Diamond Powder: A New Catalyst Support for the Polymer Electrolyte Membrane Fuel Cell, *ECS Trans.* 3 (2007) 27–36.

[11] K. Vaarmets, P. Valk, J. Nerut, I. Tallo, J. Aruväli, S. Sepp, E. Lust, Rotating Disk Electrode Study of Carbon Supported Pt-Nanoparticles Synthesized Using Microwave-Assisted Method, *ECS Trans.* 80 (2017) 743–755.

[12] E. Lust, K. Vaarmets, J. Nerut, I. Tallo, P. Valk, S. Sepp, E. Härk, Influence of specific surface area and microporosity-mesoporosity of pristine and Pt-nanoclusters modified carbide derived carbon electrodes on the oxygen electroreduction, *Electrochim. Acta* 140 (2014) 294–303.

[13] M. Yaldagard, M. Jahanshahi, N. Seghatoleslami, Carbonaceous Nanostructured Support Materials for Low Temperature Fuel Cell Electrocatalysts—A Review, *World J. Nano Sci. Eng.* 03 (2013) 121.

[14] D. Sebastián, I. Suelves, R. Moliner, M.J. Lázaro, A. Stassi, V. Baglio, A.S. Aricò, Optimizing the synthesis of carbon nanofiber based electrocatalysts for fuel cells, *Appl. Catal. B Environ.* 132–133 (2013) 22–27.

[15] X. Li, I.-M. Hsing, The effect of the Pt deposition method and the support on Pt dispersion on carbon nanotubes, *Electrochim. Acta* 51 (2006) 5250–5258.

[16] K.-Y. Chan, J. Ding, J. Ren, S. Cheng, K.Y. Tsang, Supported mixed metal nanoparticles as electrocatalysts in low temperature fuel cells, *J. Mater. Chem.* 14 (2004) 505–516.

[17] T. Mousavand, J. Zhang, S. Ohara, M. Umetsu, T. Naka, T. Adschiri, Organic-ligand-assisted supercritical hydrothermal synthesis of titanium oxide nanocrystals leading to perfectly dispersed titanium oxide nanoparticle in organic phase, *J. Nanoparticle Res.* 9 (2007) 1067–1071.

[18] H. Nagao, M. Ichiji, I. Hirasawa, Synthesis of Platinum Nanoparticles by Reductive Crystallization Using Polyethyleneimine, *Chem. Eng. Technol.* 40 (2017) 1242–1246.

[19] D. Li, C. Wang, D.S. Strmcnik, D.V. Tripkovic, X. Sun, Y. Kang, M. Chi, J.D. Snyder, D. van der Vliet, Y. Tsai, V.R. Stamenkovic, S. Sun, N.M. Markovic, Functional links between Pt single crystal morphology and nanoparticles with different size and shape: the oxygen reduction reaction case, *Energy Environ. Sci.* 7 (2014) 4061–4069.

[20] H. Yano, M. Watanabe, A. Iiyama, H. Uchida, Particle-size effect of Pt cathode catalysts on durability in fuel cells, *Nano Energy* 29 (2016) 323–333.

[21] R.K. Ahluwalia, S. Arisetty, X. Wang, X. Wang, R. Subbaraman, S.C. Ball, S. DeCrane, D.J. Myers, Thermodynamics and Kinetics of Platinum Dissolution from Carbon-Supported Electrocatalysts in Aqueous Media under Potentiostatic and Potentiodynamic Conditions, *J. Electrochem. Soc.* 160 (2013) F447–F455.
[22] K.J.J. Mayrhofer, B.B. Blizanac, M. Arenz, V.R. Stamenkovic, P.N. Ross, N.M. Markovic, The Impact of Geometric and Surface Electronic Properties of Pt-Catalysts on the Particle Size Effect in Electrocatalysis, *J. Phys. Chem. B* 109 (2005) 14433–14440.
[23] K.J.J. Mayrhofer, D. Strmcnik, B.B. Blizanac, V. Stamenkovic, M. Arenz, N.M. Markovic, Measurement of oxygen reduction activities via the rotating disc electrode method: From Pt model surfaces to carbon-supported high surface area catalysts, *Electrochim. Acta* 53 (2008) 3181–3188.
[24] M.L. Sattler, P.N. Ross, The surface structure of Pt crystallites supported on carbon black, *Ultramicroscopy* 20 (1986) 21–28.
[25] J. Tae Hwang, J. Shik Chung, The morphological and surface properties and their relationship with oxygen reduction activity for platinum-iron electrocatalysts, *Electrochim. Acta* 38 (1993) 2715–2723.
[26] F. Maillard, M. Martin, F. Gloaguen, J.-M. Léger, Oxygen electroreduction on carbon-supported platinum catalysts. Particle-size effect on the tolerance to methanol competition, *Electrochim. Acta* 47 (2002) 3431–3440.
[27] M. Peuckert, T. Yoneda, R.A.D. Betta, M. Boudart, Oxygen Reduction on Small Supported Platinum Particles, *J. Electrochem. Soc.* 133 (1986) 944–947.
[28] B. Beyribey, B. Çorbacioğlu, Z. Altin, Synthesis of platinum particles from H_2PtCl_6 with hydrazine as reducing agent, *Gazi Univ. J. Sci.* 22 (2009) 351–357.
[29] Y. Verde, G. Alonso-Nuñez, M. Miki-Yoshida, M. José-Yacamán, V.H. Ramos, A. Keer, Active area and particle size of Pt particles synthesized from $(NH_4)_2PtCl_6$ on a carbon support, *Catal. Today* 107–108 (2005) 826–830.
[30] S. Zhang, Y. Shao, X. Li, Z. Nie, Y. Wang, J. Liu, G. Yin, Y. Lin, Low-cost and durable catalyst support for fuel cells: Graphite submicronparticles, *J. Power Sources* 195 (2010) 457–460.
[31] T. Wenmao, P. Qun, L. Yanyan, W. Nan, Microcrystalline graphite oxide as durable catalyst support for PEM fuel cell, *Int. J. Electrochem. Sci.* 7 (2012) 11578–11587.
[32] M. Wang, F. Xu, H. Sun, Q. Liu, K. Artyushkova, E.A. Stach, J. Xie, Nanoscale graphite-supported Pt catalysts for oxygen reduction reactions in fuel cells, *Electrochim. Acta* 56 (2011) 2566–2573.
[33] S. Park, Y. Shao, H. Wan, P.C. Rieke, V.V. Viswanathan, S.A. Towne, L.V. Saraf, J. Liu, Y. Lin, Y. Wang, Design of graphene sheets-supported Pt catalyst layer in PEM fuel cells, *Electrochem. Commun.* 13 (2011) 258–261.
[34] R.N. Singh, R. Awasthi, C.S. Sharma, Review: An overview of recent development of platinum-based cathode materials for direct methanol fuel cells, *Int. J. Electrochem. Sci.* 9 (2014) 5607–5639.
[35] T. Li, P.B. Balbuena, Computational Studies of the Interactions of Oxygen with Platinum Clusters, *J. Phys. Chem. B* 105 (2001) 9943–9952.
[36] N.M. Marković, P.N. Ross, Surface science studies of model fuel cell electrocatalysts, *Surf. Sci. Rep.* 45 (2002) 117–229.
[37] D.K. Kinoshita, Electrochemical Oxygen Technology, John Wiley & Sons, 1992.
[38] H.S. Wroblowa, Yen-Chi-Pan, G. Razumney, Electroreduction of oxygen: A new mechanistic criterion, J. Electroanal. Chem. Interfacial Electrochem. 69 (1976) 195–201.
[39] R.J. Taylor, A.A. Humffray, Electrochemical studies on glassy carbon electrodes: III. Oxygen reduction in solutions of low pH (pH<10), *J. Electroanal. Chem. Interfacial Electrochem.* 64 (1975) 85–94.

[40] A. Damjanovic, V. Brusic, Electrode kinetics of oxygen reduction on oxide-free platinum electrodes, *Electrochim. Acta* 12 (1967) 615–628.
[41] R.J. Taylor, A.A. Humffray, Electrochemical studies on glassy carbon electrodes: II. Oxygen reduction in solutions of high pH (pH>10), *J. Electroanal. Chem. Interfacial Electrochem.* 64 (1975) 63–84.
[42] E. Yeager, Dioxygen electrocatalysis: mechanisms in relation to catalyst structure, *J. Mol. Catal.* 38 (1986) 5–25.
[43] V.P. Zhdanov, B. Kasemo, Kinetics of electrochemical O_2 reduction on Pt, *Electrochem. Commun.* 8 (2006) 1132–1136.
[44] J.K. Nørskov, J. Rossmeisl, A. Logadottir, L. Lindqvist, J.R. Kitchin, T. Bligaard, H. Jónsson, Origin of the Overpotential for Oxygen Reduction at a Fuel-Cell Cathode, *J. Phys. Chem. B* 108 (2004) 17886–17892.
[45] J. Huang, M. Eikerling, Modeling the oxygen reduction reaction at platinum-based catalysts: A brief review of recent developments, *Curr. Opin. Electrochem.* 13 (2019) 157–165.
[46] M. Markiewicz, C. Zalitis, A. Kucernak, Performance measurements and modelling of the ORR on fuel cell electrocatalysts – the modified double trap model, *Electrochim. Acta* 179 (2015) 126–136.
[47] V.R. Stamenkovic, B. Fowler, B.S. Mun, G. Wang, P.N. Ross, C.A. Lucas, N.M Marković, Improved Oxygen Reduction Activity on $Pt_3Ni(111)$ via Increased Surface Site Availability, *Science* 315 (2007) 493–497.
[48] N.M. Marković, T.J. Schmidt, V. Stamenković, P.N. Ross, Oxygen Reduction Reaction on Pt and Pt Bimetallic Surfaces: A Selective Review, *Fuel Cells* 1 (2001) 105–116.
[49] S. Gottesfeld, Electrocatalysis of Oxygen Reduction in Polymer Electrolyte Fuel Cells: A Brief History and a Critical Examination of Present Theory and Diagnostics, in: Fuel Cell Catal., John Wiley & Sons, Ltd, 2008: pp. 1–30.
[50] E. Antolini, Carbon supports for low-temperature fuel cell catalysts, *Appl. Catal. B Environ.* 88 (2009) 1–24.
[51] S. Sharma, B.G. Pollet, Support materials for PEMFC and DMFC electrocatalysts—A review, *J. Power Sources* 208 (2012) 96–119.
[52] K. Koziol, B.O. Boskovic, N. Yahya, Synthesis of Carbon Nanostructures by CVD Method, in: N. Yahya (Ed.), Carbon Oxide Nanostructures Synth. Characterisation Appl., Springer Berlin Heidelberg, Berlin, Heidelberg, 2011: pp. 23–49.
[53] S. Shanmugam, A. Gedanken, Electrochemical properties of bamboo-shaped multiwalled carbon nanotubes generated by solid state pyrolysis, *Electrochem. Commun.* 8 (2006) 1099–1105.
[54] Y. Shao, J. Liu, Y. Wang, Y. Lin, Novel catalyst support materials for PEM fuel cells: current status and future prospects, *J. Mater. Chem.* 19 (2008) 46–59.
[55] M. Beltrán-Gastélum, M.I. Salazar-Gastélum, R.M. Félix-Navarro, S. Pérez-Sicairos, E.A. Reynoso-Soto, S.W. Lin, J.R. Flores-Hernández, T. Romero-Castañón, I.L. Albarrán-Sánchez, F. Paraguay-Delgado, Evaluation of PtAu/MWCNT (Multiwalled Carbon Nanotubes) electrocatalyst performance as cathode of a proton exchange membrane fuel cell, *Energy* 109 (2016) 446–455.
[56] C. Liang, Z. Li, S. Dai, Mesoporous Carbon Materials: Synthesis and Modification, *Angew. Chem. Int. Ed.* 47 (2008) 3696–3717.
[57] M. Kim, H. Soo Kim, S. Jong Yoo, W. Cheol Yoo, Y.-E. Sung, The role of pre-defined microporosity in catalytic site formation for the oxygen reduction reaction in iron- and nitrogen-doped carbon materials, *J. Mater. Chem. A* 5 (2017) 4199–4206.
[58] A. Schlange, A.R. dos Santos, B. Hasse, B.J.M. Etzold, U. Kunz, T. Turek, Titanium carbide-derived carbon as a novel support for platinum catalysts in direct methanol fuel cell application, *J. Power Sources* 199 (2012) 22–28.

[59] C.K. Poh, S.H. Lim, H. Pan, J. Lin, J.Y. Lee, Citric acid functionalized carbon materials for fuel cell applications, *J. Power Sources* 176 (2008) 70–75.
[60] R. Roy, D. Ravichandran, A. Badzian, E. Breval, Attempted hydrothermal synthesis of diamond by hydrolysis of β-SiC powder, *Diam. Relat. Mater.* 5 (1996) 973–976.
[61] E.N. Hoffman, G. Yushin, T. El-Raghy, Y. Gogotsi, M.W. Barsoum, Micro and mesoporosity of carbon derived from ternary and binary metal carbides, *Microporous Mesoporous Mater.* 112 (2008) 526–532.
[62] Y. Gogotsi, A. Nikitin, H. Ye, W. Zhou, J.E. Fischer, B. Yi, H.C. Foley, M.W. Barsoum, Nanoporous carbide-derived carbon with tunable pore size, *Nat. Mater.* 2 (2003) 591–594.
[63] Y. Gogotsi, C. Portet, S. Osswald, J.M. Simmons, T. Yildirim, G. Laudisio, J.E. Fischer, Importance of pore size in high-pressure hydrogen storage by porous carbons, *Int. J. Hydrog. Energy* 34 (2009) 6314–6319.
[64] J. Chmiola, G. Yushin, Y. Gogotsi, C. Portet, P. Simon, P.L. Taberna, Anomalous Increase in Carbon Capacitance at Pore Sizes Less Than 1 Nanometer, *Science* 313 (2006) 1760–1763.
[65] G. Yushin, E.N. Hoffman, M.W. Barsoum, Y. Gogotsi, C.A. Howell, S.R. Sandeman, G.J. Phillips, A.W. Lloyd, S.V. Mikhalovsky, Mesoporous carbide-derived carbon with porosity tuned for efficient adsorption of cytokines, *Biomaterials* 27 (2006) 5755–5762.
[66] P. Becker, F. Glenk, M. Kormann, N. Popovska, B.J.M. Etzold, Chlorination of titanium carbide for the processing of nanoporous carbon: A kinetic study, *Chem. Eng. J.* 159 (2010) 236–241.
[67] I. Tallo, T. Thomberg, H. Kurig, A. Jänes, K. Kontturi, E. Lust, Supercapacitors based on carbide-derived carbons synthesised using HCl and Cl_2 as reactants, *J. Solid State Electrochem.* 17 (2013) 19–28.
[68] N. Batisse, K. Guérin, M. Dubois, A. Hamwi, L. Spinelle, E. Tomasella, Fluorination of silicon carbide thin films using pure F_2 gas or XeF_2, *Thin Solid Films* 518 (2010) 6746–6751.
[69] C. Portet, D. Kazachkin, S. Osswald, Y. Gogotsi, E. Borguet, Impact of synthesis conditions on surface chemistry and structure of carbide-derived carbons, *Thermochim. Acta* 497 (2010) 137–142.
[70] J. Xu, R. Zhang, J. Wang, S. Ge, H. Zhou, Y. Liu, P. Chen, Effective control of the microstructure of carbide-derived carbon by ball-milling the carbide precursor, *Carbon* 52 (2013) 499–508.
[71] J. Xu, R. Zhang, J. Wang, S. Ge, F. Wen, Hollow carbon onions with larger lattice spacing obtained by chlorination of the ball-milled SiC, Mater. Lett. 88 (2012) 168–170.
[72] M. Kormann, N. Popovska, Processing of carbide-derived carbons with enhanced porosity by activation with carbon dioxide, *Microporous Mesoporous Mater.* 130 (2010) 167–173.
[73] T. Thomberg, H. Kurig, A. Jänes, E. Lust, Mesoporous carbide-derived carbons prepared from different chromium carbides, Microporous Mesoporous Mater. 141 (2011) 88–93.
[74] I. Takahashi, S.S. Kocha, Examination of the activity and durability of PEMFC catalysts in liquid electrolytes, *J. Power Sources* 195 (2010) 6312–6322.
[75] K. Shinozaki, J.W. Zack, S. Pylypenko, B.S. Pivovar, S.S. Kocha, Oxygen Reduction Reaction Measurements on Platinum Electrocatalysts Utilizing Rotating Disk Electrode Technique II. Influence of Ink Formulation, Catalyst Layer Uniformity and Thickness, *J. Electrochem. Soc.* 162 (2015) F1384–F1396.
[76] P.J. Yunker, T. Still, M.A. Lohr, A.G. Yodh, Suppression of the coffee-ring effect by shape-dependent capillary interactions, *Nature* 476 (2011) 308–311.
[77] M. Watanabe, H. Igarashi, K. Yosioka, An experimental prediction of the preparation condition of Nafion-coated catalyst layers for PEFCs, *Electrochim. Acta* 40 (1995) 329–334.

[78] T.J. Schmidt, H.A. Gasteiger, G.D. Stäb, P.M. Urban, D.M. Kolb, R.J. Behm, Characterization of High-Surface-Area Electrocatalysts Using a Rotating Disk Electrode Configuration, *J. Electrochem. Soc.* 145 (1998) 2354–2358.
[79] U.A. Paulus, T.J. Schmidt, H.A. Gasteiger, R.J. Behm, Oxygen reduction on a high-surface area Pt/Vulcan carbon catalyst: a thin-film rotating ring-disk electrode study, *J. Electroanal. Chem.* 495 (2001) 134–145.
[80] E. Higuchi, H. Uchida, M. Watanabe, Effect of loading level in platinum-dispersed carbon black electrocatalysts on oxygen reduction activity evaluated by rotating disk electrode, *J. Electroanal. Chem.* 583 (2005) 69–76..
[81] S.S. Kocha, J.W. Zack, S.M. Alia, K.C. Neyerlin, B.S. Pivovar, Influence of Ink Composition on the Electrochemical Properties of Pt/C Electrocatalysts, *ECS Trans.* 50 (2013) 1475–1485.
[82] K. Shinozaki, J.W. Zack, R.M. Richards, B.S. Pivovar, S.S. Kocha, Oxygen Reduction Reaction Measurements on Platinum Electrocatalysts Utilizing Rotating Disk Electrode Technique I. Impact of Impurities, Measurement Protocols and Applied Corrections, *J. Electrochem. Soc.* 162 (2015) F1144–F1158.
[83] D.A. Skoog, D.M. West, F.J. Holler, S.R. Crouch, Fundamentals of Analytical Chemistry, Cengage Learning, 2013.
[84] G. Denuault, M. Sosna, K.-J. Williams, 11 - Classical Experiments, in: C.G. Zoski (Ed.), Handb. Electrochem., Elsevier, Amsterdam, 2007: pp. 431–469.
[85] J. Lipkowski, P.N. Ross, Electrocatalysis, John Wiley & Sons, 1998.
[86] N.M. Marković, H.A. Gasteiger, B.N. Grgur, P.N. Ross, Oxygen reduction reaction on Pt(111): effects of bromide, *J. Electroanal. Chem.* 467 (1999) 157–163.
[87] L.H. Brickwedde, Properties of aqueous solutions of perchloric acid, *J. Res. Natl. Bur. Stand.* 42 (1949) 309.
[88] P.I. Ravikovitch, A.V. Neimark, Characterization of nanoporous materials from adsorption and desorption isotherms, *Colloids Surf. Physicochem. Eng. Asp.* 187–188 (2001) 11–21.
[89] J. Jagiello, J.P. Olivier, 2D-NLDFT adsorption models for carbon slit-shaped pores with surface energetical heterogeneity and geometrical corrugation, *Carbon* 55 (2013) 70–80.
[90] J. Jagiello, J.P. Olivier, Carbon slit pore model incorporating surface energetical heterogeneity and geometrical corrugation, *Adsorption* 19 (2013) 777–783.
[91] M.F.C. Ladd, R.A. Palmer, Structure Determination by X-ray Crystallography, 4th ed., Springer US, 2003.
[92] L. Do Chi, S. Pham Thy, N. Phong Nguyen, V. Quan Tran, Properties of Pt/C Nanoparticle Catalysts Synthesized by Electroless Deposition for Proton Exchange Membrane Fuel Cell, *Adv. Nat. Sci. Nanosci. Nanotechnol.* 4 (2013) 035011.
[93] F.J. Nores-Pondal, I.M.J. Vilella, H. Troiani, M. Granada, S.R. de Miguel, O.A. Scelza, H.R. Corti, Catalytic activity vs. size correlation in platinum catalysts of PEM fuel cells prepared on carbon black by different methods, *Int. J. Hydrog. Energy* 34 (2009) 8193.
[94] T. Biegler, D.A.J. Rand, R. Woods, Limiting oxygen coverage on platinized platinum; Relevance to determination of real platinum area by hydrogen adsorption, *J. Electroanal. Chem. Interfacial Electrochem.* 29 (1971) 269–277.
[95] D.R. Lide, G. Baysinger, S. Chemistry, L.I. Berger, R.N. Goldberg, H.V. Kehiaian, (eds.) CRC Handbook of Chemistry and Physics, CRC Press, Boca Raton (2005).
[96] Á. Kriston, T. Xie, D. Gamliel, P. Ganesan, B.N. Popov, Effect of ultra-low Pt loading on mass activity of polymer electrolyte membrane fuel cells, *J. Power Sources* 243 (2013) 958–963.

7. ACKNOWLEDGEMENTS

First, I would like to thank the European Regional Development Fund under project TK141 "Advanced materials and high-technology devices for energy recuperation systems" (2014-2020.4.01.15-0011) and the Estonian Research Council (institutional research grant No. IUT20-13) for supporting this study. I feel grateful for getting the support from Estonian National Scholarship, Dora plus in the first year.

Secondly, I am honourable to work in the research group of Prof. Enn Lust. Besides, I would like to give special thanks to Ph.D. Jaak Nerut and Ph.D. Heili Kasuk for being my supervisors. Their tremendous help during the two years of my study pushed me upward to complete the project and gain more knowledge in both theory and practical. They spent hours and hours every week on supervising and giving advice.

Also, there are huge thanks to Ph.D. Thomas Thomberg for synthesising CDC materials and explaining the theory, Ph.D. Rasmus Palm and Miriam Koppel for measuring and explaining low-temperature nitrogen adsorption/desorption results, Ph.D. Jaak Nerut for TGA and SEM results. I am very thankful for XRD results from Ph.D. Jaan Aruväli, Institute of Ecology and Earth Science. I also give a special thanks to Ph.D. Peeter Valk for guiding and working with during Pt deposition. Ph.D. Kersti Vaarmets helped me a lot during my work. She introduced me techniques for preparing electrodes, measuring ORR and discussing. I would like to thank her for that. Thank Ph.D. Rutha Jäger for helping with resources in the laboratory. Thank Ph.D. Silver Sepp for great discussions and recommendations.

Nevertheless, I would like to thank Prof. Ivo Leito for his helps, precious advice and lectures during my two-year study. He created an extremely comfortable and helpful environment for the study program. There are special thanks to lecturers such as associated Prof. Koit Herodes, Ph.D. Martin Vilbaste, Ph.D. Uno Mäeorg, Ph.D. Tõiv Haljasorg, etc. I feel shameful because I cannot list all of the lecturers here. Thank my friends, YiJiao Yao, Ismail Sarigül, Lydia Man, Nikola Obradovic, Ho Thanh Hai Hoang, Fadillah Putri Patria and Bui Kim Ngan Nguyen. They brought me to success today.

On behalf of social life, I wish to thank Ph.D. Liis Siinor, Ph.D. Carolin Siimenson, Ph.D. Piret Pikma, Ph.D. Ove Oll and other colleagues for improving my social life at work and delicious foods. I would like to thank all my friends in Estonia for making me happier every day.

Finally, thank mom, dad, and my grandparents for supporting me both in finance and in mentality. I was lucky to have your beliefs in all my decisions.

Non-exclusive licence to reproduce thesis and make thesis public

I, **Huy Qui Vinh Nguyen**,
(*author's name*)

1. herewith grant the University of Tartu a free permit (non-exclusive licence) to:

1.1. reproduce, for the purpose of preservation, including for adding to the DSpace digital archives until the expiry of the term of copyright, and

1.2. make available to the public via the web environment of the University of Tartu, including via the DSpace digital archives, under the Creative Commons licence CC BY NC ND 3.0, which allows, by giving appropriate credit to the author, to reproduce, distribute the work and communicate it to the public, and prohibits the creation of derivative works and any commercial use of the work from ***04/06/2021*** until the expiry of the term of copyright,

Oxygen reduction on platinum nanoparticles deposited onto chromium carbide-derived carbon support,
(*title of thesis*)

supervised by: **Ph.D. Jaak Nerut** and **Ph.D. Heili Kasuk**,
(*supervisor's name*)

2. I am aware of the fact that the author retains the rights specified in p. 1.

3. I certify that granting the non-exclusive licence does not infringe other persons' intellectual property rights or rights arising from the personal data protection legislation.

author's name
18/05/2019